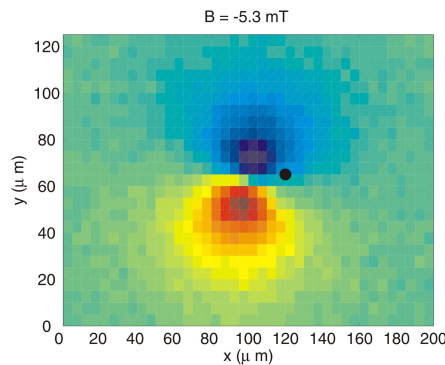


Laser-Induced Magnetization Precession in Ferromagnetic Films Grown on GaAs



A Diploma Thesis Presented by
Milan Calic

Supervised by

Gian Salis
Rolf Allenspach

IBM Zurich Research Laboratory

Silke Bühler-Paschen
Institute of Solid State Physics
Vienna University of Technology

December 2007

For my parents

Abstract

This work reports optical measurements of magnetization precession in Fe and FeCo films grown on GaAs (001) substrates. The experiments were performed by means of a pulsed laser system which enabled the time-resolved detection of ultrafast magnetization phenomena via utilization of the magneto-optical Kerr effect. Investigations of the precessional characteristics were conducted under variation of an external field applied in the plane of the film. Two-dimensional scanning images of the momentary magnetic state were taken which revealed excited regions and the direction of equilibrium magnetization. Finally, computational methods were used to fit the precession frequencies in order to gain values for the magnetic anisotropy constants.

Contents

1	Introduction	7
2	Magnetic Interactions and Magnetization Precession	8
2.1	Magnetic interactions	8
2.1.1	Exchange interaction	8
2.1.2	Zeeman Energy	9
2.1.3	Magneto-crystalline anisotropy	9
2.1.4	Shape anisotropy	9
2.2	Magnetization precession	10
2.3	Modeling an expression for the total magnetic energy	13
3	Experimental Technique and Methods of Data Analysis	15
3.1	Experimental setup: overview	15
3.1.1	Balanced photodiode bridge	17
3.1.2	Double modulation technique for lock-in detection	17
3.1.3	Sample cooling	19
3.1.4	Control over the laser focus spots	19
3.2	Laser-induced magnetization precession	19
3.2.1	Precession induced via photocurrent generation	19
3.2.2	Precession induced via anisotropy change	22
3.3	Methods of data analysis	23
3.3.1	Fitting a single TR-MOKE curve	23
3.3.2	Fitting a precession frequency spectrum	23
4	Static Properties of the Samples	25
4.1	General description of the samples	25
4.2	Static MOKE measurements	26
4.2.1	Single crystalline FeCo on GaAs	26
4.2.2	Polycrystalline FeCo on GaAs	28
4.2.3	Single-crystalline Fe on GaAs	28
4.2.4	Polycrystalline Fe on GaAs	29
5	Results from TR-MOKE measurements	32
5.1	Single crystalline FeCo on GaAs(001)	32
5.1.1	Intermediate axis characteristics	32
5.1.2	Easy axis characteristics	39

Contents

5.1.3	Numerical fits	40
5.2	Polycrystalline FeCo	43
5.3	Single crystalline Fe on GaAs(001)	44
5.3.1	Low temperature characteristics	44
5.3.2	Numerical fits	48
5.4	Polycrystalline Fe	49
6	Summary and Outlook	51
7	Acknowledgments	53

1 Introduction

The investigation of laser-induced magnetization dynamics in the time domain is a young field of research. With the development of pump-probe techniques which employ the magneto-optical Kerr-effect in pulsed laser systems, it has become feasible to generate ultrafast magnetization phenomena and to observe them on a subpicosecond timescale. In 2001, Acremann et al. [1] reported time-resolved measurements of magnetization precession in a thin FeCo film grown on a GaAs substrate, where he exploited the nature of the Schottky barrier to optically induce a local transient magnetic field in order to excite the magnetic moments. A year after that, van Kampen et al. demonstrated that a coherent precession of the magnetization can be triggered by utilizing the temperature dependence of the magnetic anisotropies in rapidly heating the sample with intense pump laser pulses [2].

In this work, time-resolved magneto-optical Kerr-effect (TR-MOKE) measurements of magnetization precession in Fe and FeCo films grown on GaAs (001) substrates were performed. The dependence of the precessional characteristics upon an external magnetic field applied in the film plane was examined. Furthermore, snap-shots of the dynamics were taken in the form of two-dimensional scanning images of the Kerr signal. Finally, results for the anisotropy constants were gained by fitting the frequency versus magnetic field curves.

After first giving an outline of magnetic interactions and magnetization precession (Chapt. 2), the experimental techniques and methods of data analysis will be explained (Chapt. 3). The investigated samples will be described and static MOKE data will be presented (Chapt. 4). Then, the results from TR-MOKE measurements will be shown and discussed together with computational evaluations (Chapt. 5). Finally, the last chapter will summarize the findings.

2 Magnetic Interactions and Magnetization Precession

2.1 Magnetic interactions

The magnetic properties of a material dramatically affect its resonance behavior in experiments where the magnetic moments are brought to precess. Hence, it might be appropriate to begin with specifying fundamental magnetic interactions which are important to understand and describe magnetization precession.

2.1.1 Exchange interaction

The long range magnetic order that is encountered in ferromagnetic materials is attributed to the exchange interaction. Through the interplay of electrostatic forces and the Pauli principle it becomes energetically more favorable for the spins to line up. The resulting interaction is referred to as exchange interaction which can be expressed for an ensemble of spins by the Hamiltonian

$$\hat{\mathcal{H}}_{exch} = - \sum_{i,j} J_{ij} \mathbf{S}_i \cdot \mathbf{S}_j \quad (2.1)$$

according to the Heisenberg model. Here \mathbf{S}_i , \mathbf{S}_j are spin operators and J_{ij} denotes the corresponding exchange integral of the i^{th} and j^{th} electron. It expresses the difference in Coulomb interaction energy when neighboring spins are aligned parallel or antiparallel with respect to each other. In case of a ferromagnet J_{ij} is positive corresponding to parallel alignment of the spins. When the discrete nature of the crystal lattice is ignored in the continuum limit, the expression for the exchange energy can be written as [3]

$$E_{exchange} = A(\nabla \mathbf{m})^2. \quad (2.2)$$

Here $\mathbf{m} = \mathbf{M}/M_s$ is the normalized magnetization and A is an exchange constant proportional to J . The exchange interaction is the force responsible for long range magnetic ordering and keeps the magnetization spatially uniform in ferromagnetic domains. Any perturbation of the spin system is accompanied by the launching of **spin waves** that exhibit quantized energies. The generation of these wavelike excitations are an important energy dissipation mechanism in ferromagnets.

2.1.2 Zeeman Energy

The potential energy of a magnetic body subject to an magnetic field \mathbf{H} is given by the Zeeman energy

$$E_{zeeman} = -\mu_0 \mathbf{M} \cdot \mathbf{H} . \quad (2.3)$$

\mathbf{M} will align with \mathbf{H} if the latter becomes large enough to overcome internal magnetic fields of a sample.

2.1.3 Magneto-crystalline anisotropy

Ferromagnetic solids possess directions along which they are easier to magnetize than others which the magnetization tends to avoid. These are referred to as **easy axes** and **hard axes**. The magnetization in domains is not arbitrarily oriented but preferably aligned with an easy axis. The reason for the magneto-crystalline anisotropy is believed to be the spin-orbit interaction: as a result of relativistic transformation an electron moving in an electric field also experiences a magnetic field. Therefore the orbital motion of an electron in the electrostatic potential of a nucleus is accompanied with an interaction between the electrons' spin and its orbital motion. The orientation and shape of electron orbitals in solids is determined by the symmetry of the crystal lattice, hence also the direction of the spins is influenced due to spin-orbit interaction. A change in the orientation of the spins (e.g. forced by an external magnetic field) will reorientate the atomic orbitals, giving rise to different overlaps of electronic wavefunctions and thus modifying the total energy of the system.

For cubic systems such as Fe magneto-crystalline anisotropy is usually expressed in form of an energy density term

$$E_{crystal} = K_1(m_x^2 m_y^2 + m_y^2 m_z^2 + m_z^2 m_x^2) + K_2 m_x^2 m_y^2 m_z^2 , \quad (2.4)$$

where K_1 and K_2 denote anisotropy constants and m_x , m_y , m_z are the components of the normalized magnetization $\mathbf{m} = \mathbf{M}/M_s$ with respect to the main crystal axes. From this definition it follows that in case $K_1 > 0$ (such as for Fe), the $\langle 100 \rangle$ directions constitute easy axes, whereas if $K_1 < 0$, then the latter directions are hard axes and the $\langle 111 \rangle$ locate the energy minima for the spatial direction of the magnetization vector [4]. The energy contributions introduced by cubic anisotropy terms are visualized in Fig. 2.1 .

2.1.4 Shape anisotropy

The long-range magnetic dipolar interaction acting between magnetic moments is the source of shape anisotropy, which is a magnetic anisotropy that depends on the geometry of ferromagnetic bodies. As a consequence of the discontinuity of \mathbf{M} at sample boundaries an effective **demagnetizing field** \mathbf{H}_{dem} builds up that opposes the magnetization. The appearance of this field results from $\nabla \cdot \mathbf{B} = 0$, so that

$$\nabla \cdot \mathbf{H}_{dem} = -\nabla \cdot \mathbf{M} . \quad (2.5)$$

The total magnetic energy can be minimized by adapting the individual alignments of the magnetic moments with respect to each other and to the boundaries so that the stray field

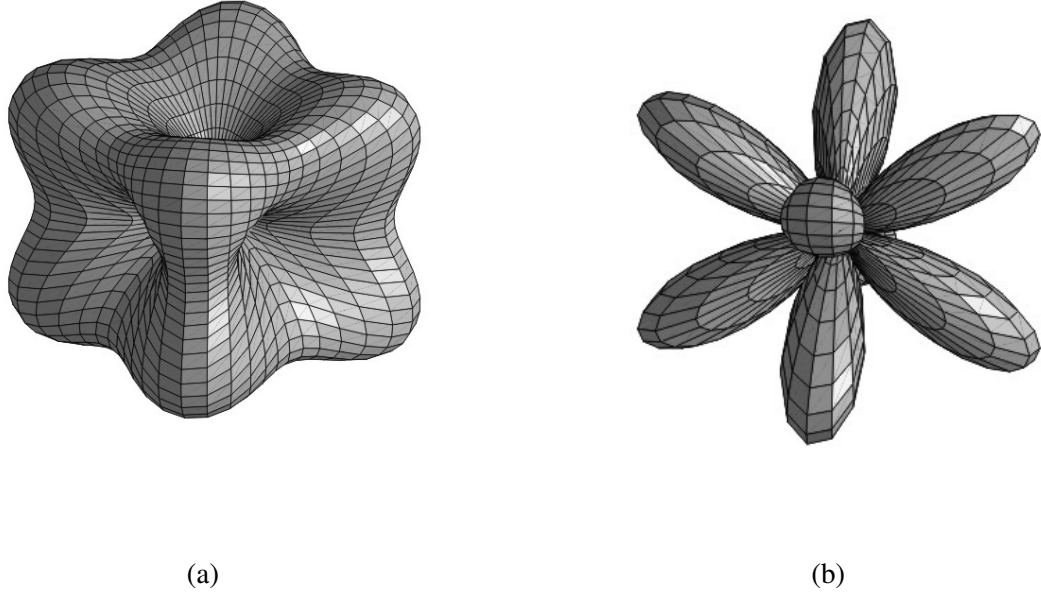


Figure 2.1: Three dimensional illustrations of the energy contributions arising from cubic anisotropy for positive K_1 and K_2 . The energy surfaces are plotted here separately for (a) the term proportional to K_1 in Equ. (2.4) and (b) the term proportional to K_2 .

generated outside of the body is reduced. The formation of domains in ferromagnetic samples is mainly caused by this effect.

As a result of shape anisotropy, the most favorable orientation of the magnetization of thin films is a direction within the film plane. If \mathbf{M} is canted out of the plane by an angle θ an additional term

$$E_{shape} = \frac{1}{2} \mu_0 M_{eff} M_s \cos^2 \theta \quad (2.6)$$

will appear in the energy density function. $M_{eff} = M_s - 2K_z/\mu M_s$ is an effective demagnetizing term that includes the stray field and a uniaxial anisotropy constant K_z which may arise e.g. from interfaces.

2.2 Magnetization precession

Only a few years ago, it was discovered that ultrashort laser pulses can be employed to induce a coherent motion of the magnetization [1, 2]. The theoretical foundations for the description of the observed precessional magnetization dynamics, however, were already established in 1935 by Landau and Lifshitz [5] and in 1955 by Gilbert [6]. If one tries to imagine the large number of magnetic moments that a ferromagnetic sample may contain and the complex interactions appearing, it may seem almost impossible to find a model that can describe the overall dynamics in such an experiment accurately. The situation is yet not as complicated if

one deals with a coherent motion of magnetic moments, because in that case the system can be simply represented by the magnetization \mathbf{M} . The dynamics can then be formulated by the non-linear differential equation

$$\frac{d\mathbf{M}}{dt} = -\gamma\mu_0 (\mathbf{M} \times \mathbf{H}_{eff}) + \frac{\alpha}{M_S} \left(\mathbf{M} \times \frac{d\mathbf{M}}{dt} \right). \quad (2.7)$$

This is known as the **Landau-Lifschitz-Gilbert (LLG) equation**. It describes the damped precessional motion of \mathbf{M} around an effective field \mathbf{H}_{eff} (Fig. 2.2). The expression

$$\frac{d\mathbf{M}}{dt} = -\gamma\mu_0 (\mathbf{M} \times \mathbf{H}_{eff}). \quad (2.8)$$

represents a precessional motion of magnetization in space. The reason why \mathbf{M} precesses at all instead of simply turning towards the effective magnetic field \mathbf{H}_{eff} arises from the fact that each magnetic moment $\boldsymbol{\mu}$ is coupled to an angular momentum \mathbf{L} by the relation

$$\boldsymbol{\mu} = \gamma \mathbf{L}. \quad (2.9)$$

$\gamma = g\mu_B/\hbar$ is the gyromagnetic ratio. The precessional motion follows from this because the torque $\mathbf{M} \times \mathbf{H}_{eff}$ exerted upon \mathbf{M} must be equal to the rate of change of total angular momentum:

$$\mathbf{M} \times \mathbf{H}_{eff} = \frac{d}{dt} \left(\sum_i L_i \right) = \frac{d}{dt} \left(\frac{1}{\gamma} \mathbf{M} \right). \quad (2.10)$$

In order to account for energy dissipation, a damping term has to be included into the previous equation. By choosing this term to have the form

$$\frac{\alpha}{M_S} \left(\mathbf{M} \times \frac{d\mathbf{M}}{dt} \right) \quad (2.11)$$

with the phenomenological damping parameter $\alpha \leq 1$, one arrives at the LLG equation. α is connected to the time scale τ of exponential relaxation via the precession frequency ω :

$$\tau = \frac{1}{\alpha\omega} \quad (2.12)$$

The microscopic mechanisms responsible for the inherent damping are assumed to be mediated by direct coupling to the lattice via spin-orbit interaction, indirect coupling via spin-waves, impurity relaxation mechanisms and eddy currents [7].

As one might assume, the effective field around which \mathbf{M} precesses is not just given by an external field applied to the magnetic body. When no external field is present, \mathbf{M} will be oriented such that the magnetic energy contributions of crystalline and shape anisotropies are minimized. If \mathbf{M} is deflected from that direction by a short excitation, then the anisotropies will give rise to restoring torques. The subsequent damped precessional motion of \mathbf{M} towards its equilibrium direction can be consistently described with Equ. (2.7) if one associates the energy terms of the anisotropies with magnetic fields [8]. \mathbf{H}_{eff} is then given by the sum of these "anisotropy fields".

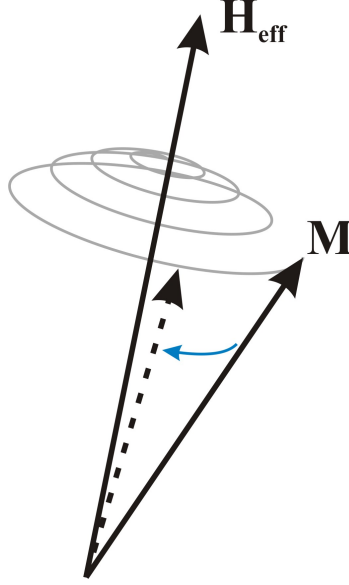


Figure 2.2: Damped precessional motion of the magnetization vector \mathbf{M} around an effective field \mathbf{H}_{eff} , as described by the LLG equation Equ. (2.7). Equilibrium will be reached when the condition $|\mathbf{M} \times \mathbf{H}_{eff}| = 0$ is met.

The magnetic energies can be related to an effective field by calculating the functional derivative of the total magnetic energy density E_{tot} :

$$\mathbf{H}_{eff} = -\frac{1}{\mu_0} \frac{\partial E_{tot}}{\partial \mathbf{M}} . \quad (2.13)$$

\mathbf{H}_{eff} includes all magnetic contributions for the general case when an external magnetic field is also present. E_{tot} is given by the sum of Zeeman, shape, magneto-crystalline and exchange energy:

$$E_{tot} = E_{zeeman} + E_{shape} + E_{crystal} + E_{exchange} . \quad (2.14)$$

From this energy expression it is also possible to determine the eigenfrequency of the uniform precession mode using the formula [9]

$$\omega = \frac{\gamma}{M_s \sin \theta} \sqrt{\frac{\partial^2 E_{tot}}{\partial \theta^2} \frac{\partial^2 E_{tot}}{\partial \phi^2} - \left(\frac{\partial^2 E_{tot}}{\partial \theta \partial \phi} \right)^2} , \quad (2.15)$$

which can be derived from the LLG equation in spherical coordinates for small deviations of \mathbf{M} from equilibrium. The azimuthal angle ϕ and the polar angle θ specify the direction of the magnetization \mathbf{M} when it is in equilibrium with \mathbf{H}_{eff} . An important conclusion can be drawn in connection to the formula for the precession frequency, namely that ω is determined by the curvature of the energy landscape at the minimum of total energy.

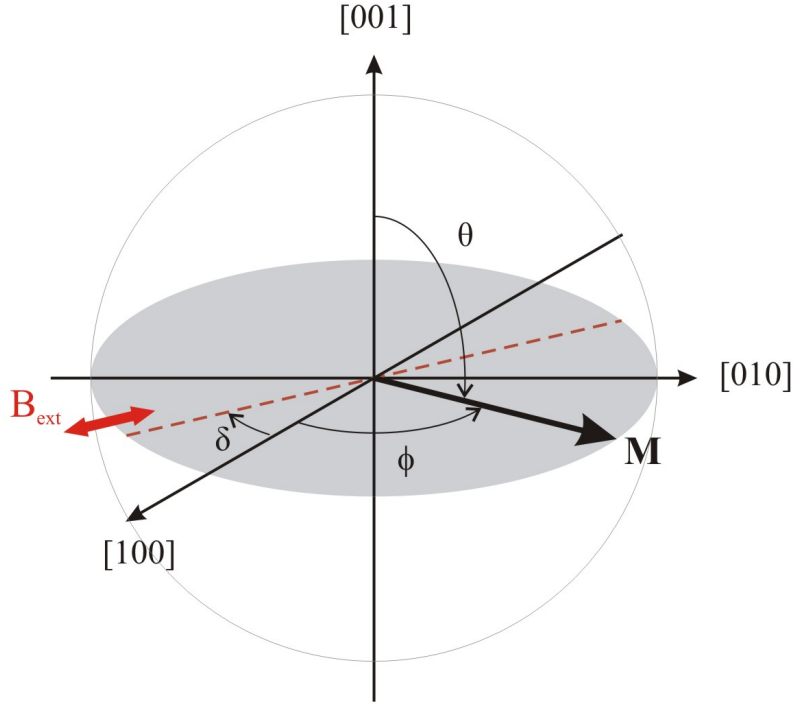


Figure 2.3: Coordinate system corresponding to the model for the total energy in Equ. (2.16).

2.3 Modeling an expression for the total magnetic energy

The eigenfrequency ω of the uniform precessional mode of magnetic moments is correlated to the total magnetic energy E_{tot} via Equ. (2.15). Consequently, if an appropriate expression for E_{tot} can be formulated for a specific sample, then an observed frequency spectrum - i.e., magnetization precession frequency as a function of magnitude of an external field - should be computable [10]. This can actually be achieved by tailoring E_{tot} for a given thin film sample by considering carefully which magnetic contributions may play a role in the dynamics of magnetization precession. By making use of the knowledge about the different magnetic energy terms presented above in this text, one can generally assume that there must be a Zeeman term, a shape anisotropy term, a crystalline anisotropy term and an exchange energy term in the total energy. Furthermore, one has to take into account the specific properties of the sample for which E_{tot} is to be modeled. In our case this meant that we had to include an energy term which accounted for a uniaxial in-plane anisotropy.¹ Finally, all of these terms have to be expressed in a convenient coordinate system and be merged together. Following these steps,

¹Our samples exhibited a uniaxial anisotropy in addition to their crystalline anisotropy (will be described later in this text).

we arrived at the energy formula

$$\begin{aligned}
 E_{tot} = & - \underbrace{|\mathbf{B}_{ext}| M_s \cos(\phi - \delta) \sin \theta}_{\text{Zeeman}} + \underbrace{K_u \sin^2 \theta \sin^2(\phi - \epsilon)}_{\text{Uniaxial anisotropy}} + \underbrace{\frac{1}{2} \mu_0 M_{eff} M_s \cos^2 \theta}_{\text{Shape anisotropy}} \\
 & + \underbrace{K_1 \left(\frac{1}{4} \sin^2 \theta \sin^2(2\phi) + \cos^2 \theta \right) \sin^2 \theta + \frac{K_2}{16} \sin^2(2\phi) \sin^2(2\theta) \sin^2 \theta}_{\text{Cubic anisotropy}} .
 \end{aligned} \tag{2.16}$$

The coordinate system which we chose is displayed in Fig. 2.3. As one can see there, θ and ϕ designate the polar and the azimuthal angle which define the spatial position of the magnetization vector \mathbf{M} with respect to the cubic crystal directions $\langle 100 \rangle$, and δ specifies the angle of application direction of the external field within the (001) plane. The latter plane constitutes the plane of a magnetic material film. The shape anisotropy term in the above equation therefore reflects the strong preference of the magnetization to adopt an orientation within the film plane. Since the easy magnetization direction of uniaxial anisotropy differed from sample to samples, it is not displayed in the figure in order not to convey a misleading image. However, its angle ϵ with respect to the [100] axis is incorporated in the corresponding energy term. K_u is the uniaxial anisotropy constant and has the same units as K_1 and K_2 (J/m³).

Not out of forgetfulness, but because of physical reasoning, the exchange interaction term was omitted. This was justified by the fact that (according to Equ. (2.2)) exchange energy only builds up if the magnetization distribution deviates from uniformity; in laser-induced magnetization precession experiments, however, experimental evidence suggests a uniform precession of the magnetic moments [1, 2, 10–12]. It should nevertheless be emphasized that the exchange interaction is the governing force which provides for the parallel coupling between neighboring magnetic moments.

The importance of Equ. (2.16) will be clarified in the results chapter, where measured dependencies of ω upon an external magnetic field will be compared with numerical calculations.

3 Experimental Technique and Methods of Data Analysis

The measurement of magnetization dynamics is an established field of research. Methods such as ferromagnetic resonance absorption via microwave fields (FMR), electron spin resonance (ESR) and nuclear magnetic resonance (NMR) have found various applications. These are however non-local techniques and measure absorption spectra in the frequency domain. Information on damping can not be obtained directly but from the broadening of absorption lines. More recently, optical methods have been developed which use pulsed laser systems. In contrast to the other mentioned techniques they enable to detect magnetization precession locally and in the time domain. The time resolution is basically restricted by the temporal length of the laser pulses which can be tuned down to femtoseconds, making the study of ultrafast dynamic phenomena possible.

The optical detection of the magnetic state with the help of lasers typically relies on a magneto-optical phenomenon called **Kerr effect**. When linearly polarized light is incident onto the surface of a magnetic sample, the reflected light experiences a rotation in its polarization axis. It is found that the rotation angle, referred to as the **Kerr angle** θ_K , is linearly related to magnetization. This property has its origin in spin-orbit coupling and optical selection rules. The Kerr effect has found applications in the study of a broad range of static magnetic properties and also in magnetic recording techniques. It can be adopted for both static (aided by continuous lasers) and dynamic (aided by pulses lasers) measurements.

Conceivably, laser systems that are able to generate ultra-short light pulses of exact shape and intensity and at high repetition rates are enormously useful for the investigation of magnetization dynamics. After a given delay Δt after magnetization precession has been excited in a ferromagnet, a single polarized laser pulse reflected from the surface can obtain information about the momentary magnetic state via Kerr rotation. One can thus measure the dynamics by continuously varying the delay Δt and detecting the Kerr angle θ_K . An experiment of this type investigates the so-called **time-resolved magneto-optical Kerr effect (TR-MOKE)**. The following sections will explain how this technique was realized in this work.

3.1 Experimental setup: overview

The experimental setup used in this work is illustrated in Fig. 3.1. A commercial Ti:sapphire mode-locked laser system with tunable wavelength provides pulses of ~ 3 ps duration at a repetition rate of 80 MHz. The light beam is split into a "pump" and a "probe" beam that have distinct purposes. The former serves as a trigger of magnetization precession whereas the latter is used to detect magnetization changes. The probe pulses are linearly polarized so they can

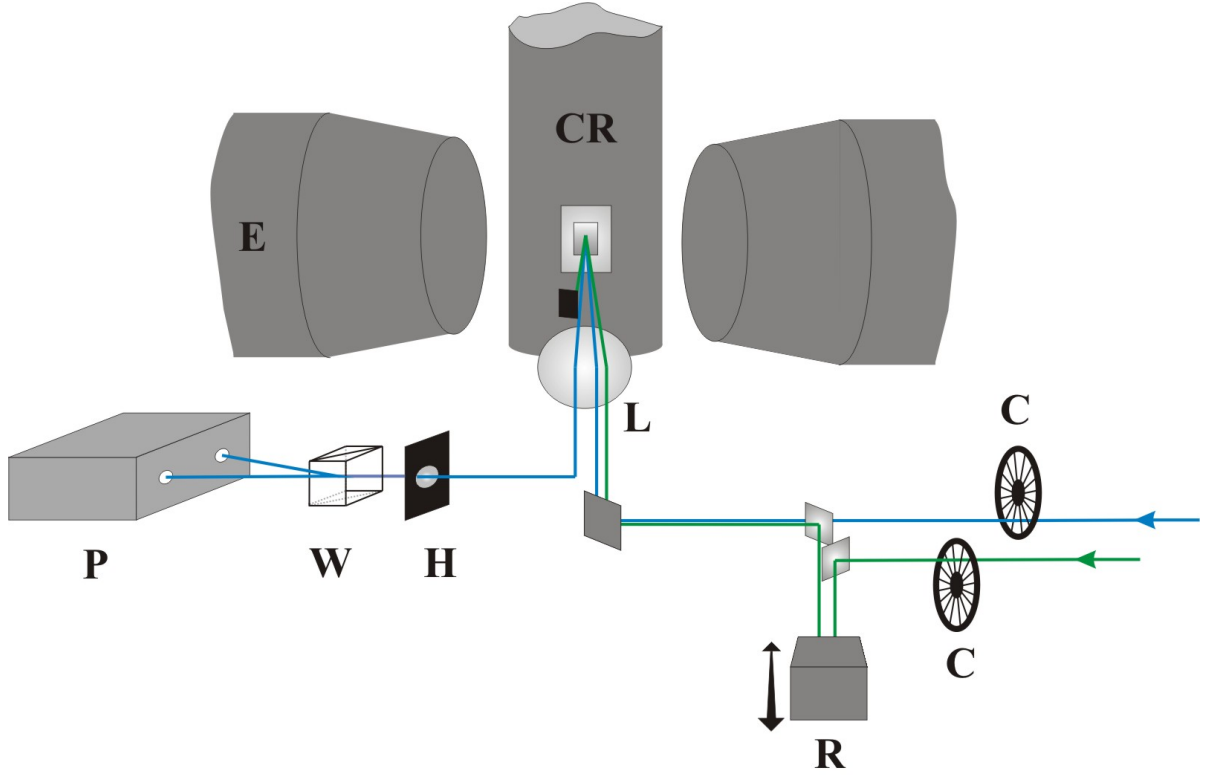


Figure 3.1: Schematic illustration of the all-optical experimental setup for both the generation and the detection of magnetization precession. C = chopper, R = retro-reflector, L = lens, CR = cryostat, E = electromagnet, H = half wave plate, W = Wollaston prism, P = photodiode box. The pump beam is represented as a green line and the probe beam as a blue line. The sample is mounted on a post within the cryostat and is accessible to the beams via a quartz window. The position of the cryostat is controllable in all three spatial dimensions by means of motors in order to scan the surface area of the sample and to perform focusing adjustments.

be utilized for the detection of the momentary magnetization via the observation of the Kerr rotation angle θ_K of their polarization upon reflection from a ferromagnetic material. Since the probe beam is incident almost perpendicularly onto the sample surface, θ_K is mainly sensitive to the out-of-plane component of the magnetization (polar MOKE geometry, see e.g. [13]).

The time delay between the pump and the probe pulses can be precisely controlled by varying their optical path difference before they reach the sample. This is achieved by introducing a retro-reflector mounted on a motorized linear stage in the path of the pump beam. Both pump and probe are focused onto the sample surface by a lens. After being reflected, the pump beam is blocked and the collimated probe beam is directed into a detection line. Here it is processed by a balanced photodiode bridge. The final signal is then fed to two lock-in amplifiers which are referenced to the probe respectively the pump beam chopper.

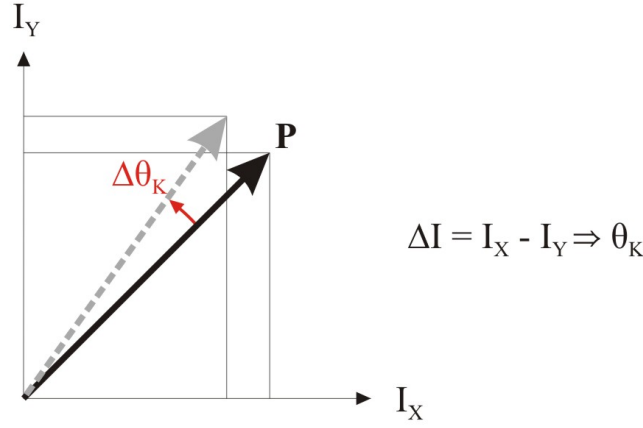


Figure 3.2: The axes of this diagram denote the two photodiode currents I_X and I_Y which correspond to the projections of the polarization onto the vertical y axis and the horizontal x axis as constituted by the Wollaston prism. The bold and the dashed arrow illustrate the polarization P before and after a change in magnetization, respectively. The difference $\Delta I = I_X - I_Y$ is directly related to the Kerr rotation angle θ_K , thus holding information about the momentary magnetization.

3.1.1 Balanced photodiode bridge

The main purpose of using a balanced photodiode bridge in the detection system is to decrease laser noise. It consists of a motor-driven rotatable half wave plate, a Wollaston prism and a box holding two photodiodes. A half wave plate is a birefringent crystal that rotates the polarization axis of linearly polarized light. The Wollaston prism splits the incoming light into two beams which consist of the vertically and horizontally polarized component of the original beam, respectively. By this means the separated beams generate currents in the photodiodes which contain information about the particular projections (as defined by the Wollaston prism) of the polarization. By measuring the difference in photocurrents $\Delta I = I_X - I_Y$ as a function of time, variations in the momentary magnetization via changes in the magneto-sensitive Kerr rotation angle $\Delta\theta_K$ can be detected (Fig. 3.2). The photodiode box first converts ΔI into a voltage using an amplifying I/V converter before passing the signal to lock-in amplifiers.

3.1.2 Double modulation technique for lock-in detection

The voltage signal provided by the photodiode box is processed by two lock-in amplifiers. The first amplifier directly receives the signal (transmitted via a coaxial cable) and is referenced to the optical chopper modulating the pump beam at a high frequency, $f_{pump} \approx 3$ kHz. The second one, being referenced to the low frequency of the probe beam chopper ($f_{probe} \approx 300$ Hz), analyzes the output signal V_1 given by the first lock-in amplifier. In doing so, the resulting signal V_2 will be cleaned from noise arising from pump laser pulses which have been scattered into the detection line (see Fig. 3.3). In principle it would also be possible to measure the MOKE signal by using just one lock-in amplifier, but the mentioned light scattering effects would make a detection difficult, if not infeasible.

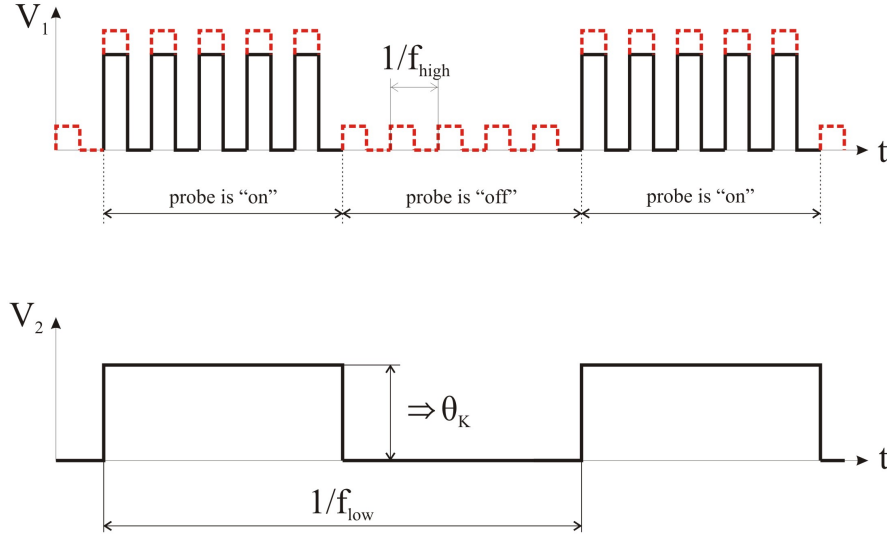


Figure 3.3: The first graph shows the double-modulated voltage signal V_1 detected by the lock-in amplifier which is referenced at the high pump beam chopper frequency f_{pump} . Whenever the probe beam is "on" (i.e. its chopper is not blocking the light), a periodically oscillating voltage consisting of the pure signal (bold black line) superposed by noise (red dashed line) is measured. When the probe beam is "off", a finite voltage will still be present because the noise which originates from scattered pump laser light is also modulated with f_{pump} . In order to get rid of this unwanted side effect, V_1 is fed into a second lock-in amplifier referenced to the low probe beam chopper frequency f_{probe} . The amplitude of the final signal V_2 is then proportional to the Kerr angle θ_K and carries much less parasitic information than in a setup which does not employ the double-modulation technique.

3.1.3 Sample cooling

Magnetization dynamics depends on temperature. On a low temperature scale some effects might be observable in a purified form due to reduced phonon scattering and a less broadened Fermi distribution. In order to conduct low temperature measurements the samples were mounted in an optical cryostat. The samples were attached and thermally connected to a post (made of copper) which was cooled by the continuous flow of liquid helium. A heater provided the possibility to regulate the temperature to a desired value between 4.2 K and 325 K, which could be controlled by means of a temperature sensor. The cold post was isolated from ambient temperature influences in a vacuum chamber and was equipped with a metallic shield against heat radiation. Using a turbomolecular pump the pressure within the cryostat was reduced to typically 10^{-6} mbar.

3.1.4 Control over the laser focus spots

The ability to precisely control the relative positions of the pump and the probe focus spots on a sample surface is essential to the detection of the time-resolved Kerr signal. A high resolution positioning method, using a tilting mirror in the optical path of the pump beam with remotely controllable micrometer actuators, was therefore incorporated in the laser setup. This made it much easier to find a "good" signal, which could be very tricky if performed manually. Secondly it became feasible to perform two-dimensional image scanning of the TR-MOKE signal at a specific delay after pump excitation. The latter was very valuable for the visualization of areas where magnetization precession occurred, as it will be presented in the results chapter.

3.2 Laser-induced magnetization precession

At the beginning of the previous section it was briefly mentioned that the excitation of a precession is established with the aid of laser pulses. In fact there are two ways to excite a coherent magnetic motion in thin ferromagnetic films with a laser. One exploits the temperature dependence of magnetic anisotropy, the other relies on the generation of a photocurrent across the growth direction of the material layer. These trigger mechanisms differ from each other but however show the same characteristics in measurements of the precession frequency as a function of a static external field. This section provides an outline of the two effects.

3.2.1 Precession induced via photocurrent generation

When a metal is brought into contact with a semiconductor a Schottky contact is formed. The energy bands of the semiconductor become bent at the interface in order to establish equilibrium of the Fermi energy levels. By applying an external voltage to the structure, the potential barrier and the charge depletion region can be modified. A Schottky contact has a pronounced rectifying behavior since a positive bias applied to the metal produces a large current whereas a negative bias closes the valve for the flow of electrons.

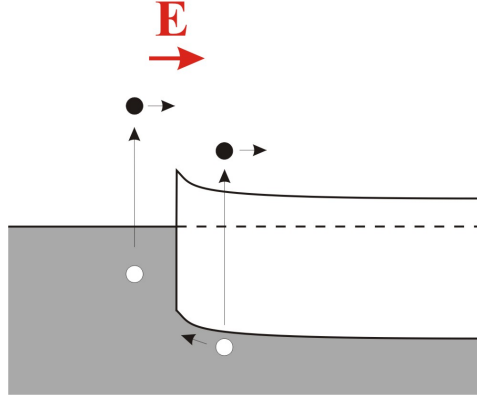


Figure 3.4: Illustration of the optical electron-hole excitation in the energy band diagram of a Schottky contact. The electrons (filled circles) are dragged towards the semiconductor region and holes (empty circles) are injected into the ferromagnet due to the intrinsic electric field \mathbf{E} in the barrier region.

At equilibrium (no bias applied) the net current across a metal-semiconductor junction is zero. However, a photo-induced current can be generated by optically exciting (e.g. by the means of a laser) electron-hole pairs in the junction [1]. Holes are then injected into the metal and electrons are conveyed towards the semiconductor due to the strong built-in potential of the energy barrier (Fig. 3.4). By either forward- or reverse-biasing the diode one can control the magnitude of the resulting photocurrent.

Since moving charges are sources of magnetic fields, the photocurrent is accompanied with a circular magnetic field that acts in the plane of the ferromagnetic film. A single laser pulse can thus produce a transient magnetic field pulse \mathbf{H}_{pulse} in a sample such as depicted in Fig. 3.5(a), provided that the thickness of the magnetic metal layer is smaller than the optical penetration depth in order that the photons can reach the semiconductor. Due to its origin in a photocurrent the field pulse described above will be referred to in short as **photocurrent field pulse** in the following text. Depending on the orientation of the magnetic moments relative to the field lines and the local strength of \mathbf{H}_{pulse} (i.e. depending on the magnitude $|\mathbf{M} \times \mathbf{H}_{pulse}|$), a variably strong torque will act (Fig. 3.5(b)). In this manner the moments are brought out of equilibrium rapidly and in a well-defined way, leading to a uniform precession of the magnetization around the effective field [1, 14]. In areas where the field lines of \mathbf{H}_{pulse} are parallel or antiparallel to the magnetic moments, the torque is zero, leaving the moments unperturbed. Regions with opposite sign in torque are identified by opposite initial conditions for precession, which means that the magnetic moments are initially tipped either upwards or downwards with respect to the sample plane before they start their damped precessional motion towards equilibrium. This issue is displayed in Fig. 3.6. An important conclusion can be drawn from the geometry established by a photocurrent field pulse: The asymmetry in the sign of the torque between two half planes which is introduced by photocurrent field pulse must be reflected in different phases of precession.

Since the intensity profile of a laser pulse is Gaussian-shaped and restricted to a finite area, the magnetic field strength can be estimated to be a function of $1/r$ (with distance r from

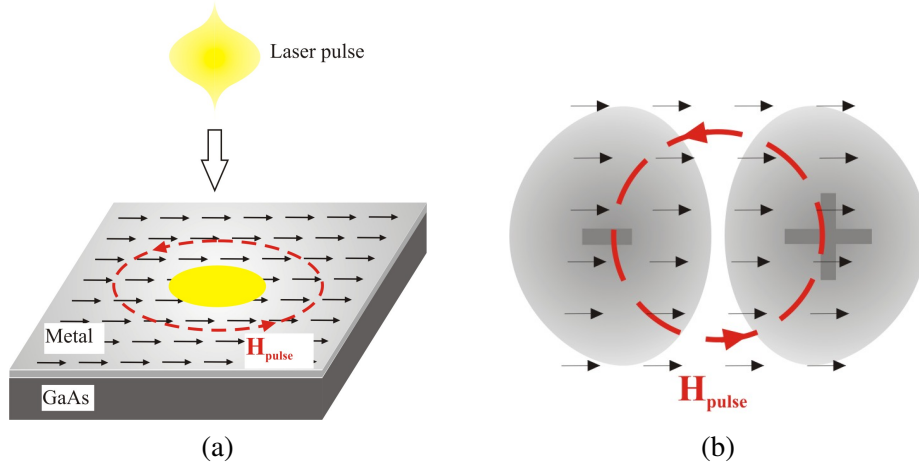


Figure 3.5: **(a)** Generation of a pulsed circular magnetic field H_{pulse} illustrated in a tilted top view onto a uniformly magnetized region of a sample. The arrows depict magnetic moments. An incident Gaussian-shaped laser pulse (yellow) penetrates the surface and causes the generation of a photocurrent perpendicularly across the Schottky barrier, which in turn is accompanied by a circular magnetic field H_{pulse} oriented within the film plane. **(b)** Top view onto the sample plane. The magnetic moments are shown here in their equilibrium orientation (arrows). Areas characterized by deflections of the magnetic moments from equilibrium are highlighted in gray. The + and - symbols indicate the difference in sign of the acting torque.

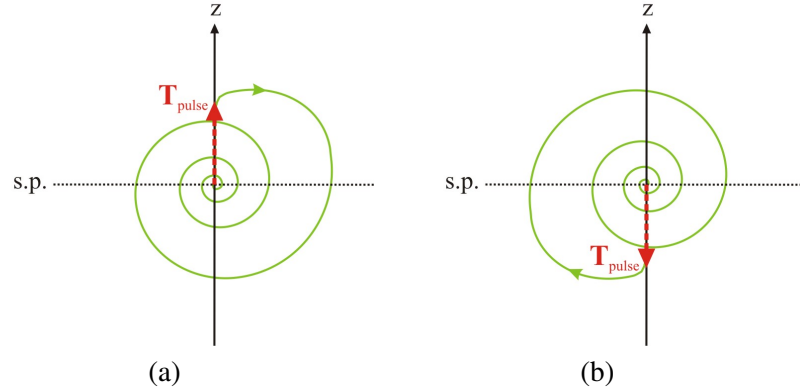


Figure 3.6: Illustrations of the difference in motion of the magnetization vector within the gray-highlighted regions of Fig. 3.5(b), where **(a)** and **(b)** represent the situation in the regions marked with "+" and "-", respectively. The magnetization is pointing out of the image plane here. T_{pulse} denotes the initiating torque which tips the magnetization out of its equilibrium position in the sample plane (denoted by s.p.). The spiral trajectory indicates how the magnetization is pulled out of its equilibrium orientation subsequent to the excitation by T_{pulse} , and proceeds with a damped precessional motion according to the LLG equation.

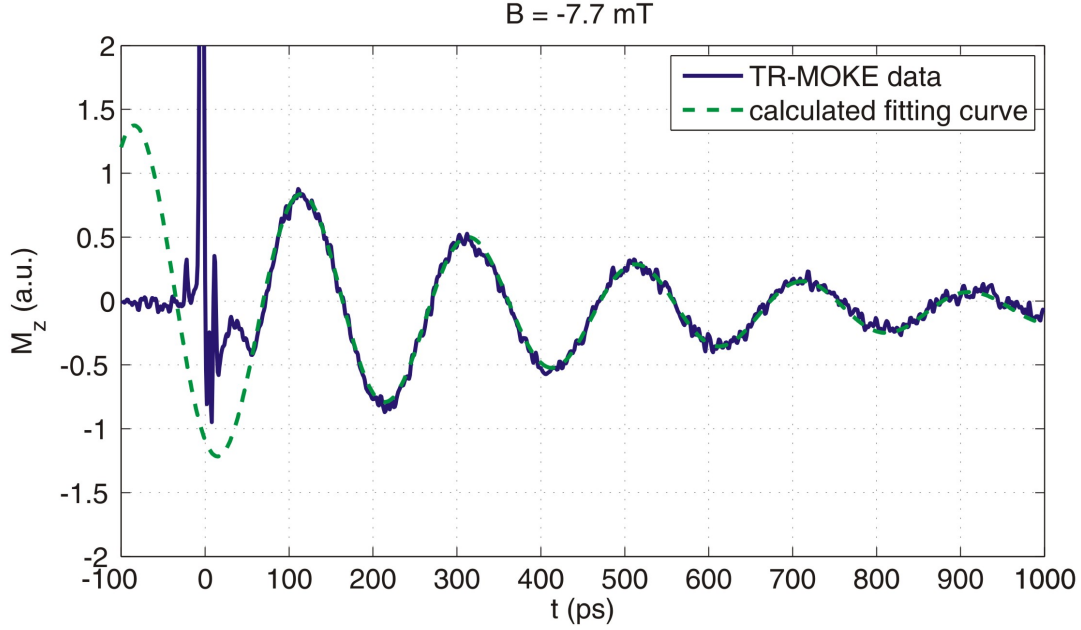


Figure 3.7: Graph showing a typical TR-MOKE signal and a fitting curve of the oscillating out-of-plane magnetization component M_z as a function of delay between the incidence of the pump pulse (excitation at $t = 0$) and the probe pulse (detection of the momentary value of M_z at a specific time after excitation), as observed in a FeCo sample.

the center) in the region outside of the pulse impact area, whereas inside the impact area the magnitude of H_{pulse} will rise linearly with r .

3.2.2 Precession induced via anisotropy change

Another way of inducing a magnetization precession is to exploit the temperature dependence of the magnetic anisotropies [2, 11, 12]. The absorption of an intense laser pulse heats up the electrons in the ferromagnetic sample and leads to an expansion of the crystal lattice. Due to spin-orbit interaction the anisotropies are changed instantaneously, causing a perturbation of the magnetic moments. Subsequently the magnetization begins a damped precessional motion around the effective field. Due to this effect involved upon the sudden change of anisotropy this triggering mechanism is referred to as **anisotropy field pulse**.

It should be noted that another important factor for initiating a precession is assumed to be the ultrafast demagnetization which occurs in the first few hundreds of femtoseconds after laser excitation [11, 15].

3.3 Methods of data analysis

3.3.1 Fitting a single TR-MOKE curve

Fig. 3.7 shows a graph of typical TR-MOKE data. The observed signal characteristics is equivalent to the motion of a weakly damped harmonic oscillator. Taking into account that only the out-of-plane component M_z of film magnetization is probed in the polar MOKE geometry (i.e. the probe beam is directed in a nearly right angle onto the sample surface), the temporal evolution of the magnetization signal can be described with

$$M_z(t) = M_0 e^{-\tau/t} \cos(\omega t + \Delta\Phi) . \quad (3.1)$$

By fitting a measured data curve to this expression, parameters which characterize the oscillation (and therefore the magnetization dynamics) can be extracted. These are the initial oscillation amplitude M_0 , the exponential decay time τ , the angular precession frequency of the magnetic moments ω and the phase $\Delta\Phi$ of the oscillation. Our fitting routine consisted of two steps:

1. Choose initial values for ω , $\Delta\Phi$, τ and M_0 to calculate $M_z(t)$ via Equ. (3.1)
2. Adapt $M_z(t)$ to the measured curve by employing a multidimensional optimization method which finds the correct values for the dynamic parameters.

This procedure for the analysis of the measurement data was implemented in the computing software MATLAB, which amongst others provides a very useful function named "fminsearch" as a computational tool for finding the minimum of a multivariable scalar function [16]. In our case, the standard deviation between the measured and calculated function values of $M_z(t)$ was minimized with "fminsearch".

3.3.2 Fitting a precession frequency spectrum

An integral part of our experimental investigations consisted in examining the influence of an external field B_{ext} on the precessional magnetization dynamics. In the results chapter, graphs will be presented which show how ω , $\Delta\Phi$, τ and M_0 vary as a function of B_{ext} applied along a certain direction. In particular, the observed frequency spectra - i.e. the graphs showing precession frequency versus B_{ext} - of a given sample reflect its magnetic anisotropies. In the second chapter of this text, it was stated that the precession frequency of the magnetization is determined (via Equ. (2.15)) by the total magnetic energy E_{tot} , which again consists on sample-intrinsic magnetic energy contributions. There, we formulated an expression for E_{tot} specifically for our thin film samples (Equ. (2.16)). This enabled us to fit the measured frequency spectra by choosing the anisotropy constants K_u , K_1 , K_2 and the effective demagnetization term M_{eff} as free parameters. Our fitting procedure for the determination of K_u , K_1 , K_2 and M_{eff} was as follows:

1. Specify the direction along which the external field B_{ext} is applied

3 Experimental Technique and Methods of Data Analysis

2. Choose initial values for K_u , K_1 , K_2 and M_{eff} ; specify a set of values for \mathbf{B}_{ext} (corresponding to measurement data)
3. Evaluate the minimum of E_{tot} (via Equ. (2.16)) for each value of \mathbf{B}_{ext} by optimizing the angles θ and ϕ in order to specify the spatial equilibrium direction of the magnetization vector \mathbf{M} .
4. Determine the second partial derivatives of E_{tot} for the equilibrium angles θ_{equ} and ϕ_{equ} , then compute the precession frequency ω from Equ. (2.15).
5. Perform a multidimensional optimization for the values of the free parameters K_u , K_1 , K_2 and M_{eff} incorporating steps 1. to 3. by minimizing the standard deviation between the calculated and the measured frequencies.

The search for the minimum of E_{tot} (step 2) was performed by the function "fminunc" of MATLAB. It also served us as a tool to numerically approximate the Hessian matrix for E_{tot} , which contains the second partial derivatives necessary to determine ω from Equ. (2.15). Step 4 of our fitting procedure was realized by using the function "fminsearch".

4 Static Properties of the Samples

4.1 General description of the samples

Crystalline semiconductor materials have proven to be extremely useful substrates for the epitaxial growth of magnetic films. For example, bcc Fe and FeCo can be grown with high quality on the zincblende structure of GaAs (001) wafers using molecular beam epitaxy (MBE) techniques on account of the very good match in lattice constants. Samples with such material combinations were investigated in this work (listed below in Tab. 4.1). The magnetic films were grown epitaxially and under ultra-high vacuum conditions on the (001) surface of arsenic-passivated GaAs wafer crystals. The wafers were n-doped with a concentration of $5 \cdot 10^{16} \text{ cm}^{-3}$. A cap layer of aluminium deposited on top of the films served as a protection against corrosion and contamination. Ohmic indium contacts were mounted at the bottom of the substrates in order to enable the application of a bias across the Schottky contact. The dimensions of the substrates were approximately $8 \text{ mm} \cdot 6 \text{ mm} \cdot 0.5 \text{ mm}$, on top of which the magnetic layers were deposited in a circular area of $\sim 3 \text{ mm}$ diameter. The samples were mounted onto ceramic sample holders which could fit into the chip socket of the cryostat.

Two different FeCo/GaAs(001) samples were examined in order to investigate the role of anisotropies in the dynamic magnetic response from TR-MOKE measurements. The first sample was characterized by a 6 nm epitaxial layer of $\text{Fe}_{30}\text{Co}_{70}$ (~ 42 monolayers), whereas the second one (sample As40) had a 1.5 nm thin Al layer in between the GaAs substrate and the FeCo. The Al interlayer had the purpose of introducing disorder (polycrystallinity) in the growth structure of the FeCo film and thereby eliminating magnetic contributions arising from cubic crystalline anisotropy. In addition, two different Fe/GaAs(001) samples were used. The first sample (As10) consisted of 9 nm epitaxial Fe, while the second (As41) was distinguished by 6 nm of polycrystalline Fe (again realized by a 1.5 nm Al interlayer).

Epitaxially grown thin films of magnetic metals have different properties than the bulk material due to their two-dimensional shape and interface effects. Their magnetization strongly favors the in-plane direction because of shape anisotropy. Furthermore it is known that Fe and FeCo films grown on GaAs exhibit a uniaxial anisotropy which superposes their cubic anisotropy. The nature of this property has not yet been understood in detail, but it is certain to arise from the symmetry break at the interface (transition from zincblende symmetry of GaAs to cubic symmetry Fe or FeCo) [4]. In fact, the presence of a uniaxial anisotropy was observed in the hysteresis loops of all of the samples listed in Tab. 4.1, even in the polycrystalline ones.

The structure of the (001) surface of GaAs is characterized by a square lattice and a distance of 5.65 \AA between the atom sites. Bulk Fe and FeCo are naturally well suited for epitaxial growth on top of GaAs (001), owing to their lattice constants which are nearly half the amount the GaAs lattice constant. Such material combinations have been examined before by means of

4 Static Properties of the Samples

Sample label	Layer sequence and widths	Cubic easy axes	Uniaxial easy axis
As10	9 nm Fe, 4 nm Al	$\langle 100 \rangle$	$[110]$
As41	1.5 nm Al, 6 nm Fe, 2 nm Al	-	-
As48	6 nm Fe ₃₀ Co ₇₀ , 3.5 nm Al	$\langle 110 \rangle$	$[110]$
As40	1.5 nm Al, 6 nm Fe ₃₀ Co ₇₀ , 2 nm Al	-	-

Table 4.1: List of investigated samples. GaAs was used as a substrate in each case. While the magnetic films of As10 and As48 were single crystalline, the samples As40 and As41 exhibited polycrystalline layers.

X-ray analysis and electron diffraction techniques [4, 17, 18]. From those investigations it was discovered that Fe and FeCo attain a bcc structure during epitaxial growth on GaAs. Moreover, the crystal axes of the films and the substrates were found to be parallel to each other. Hence, the crystal directions of the ferromagnetic films could be determined from the orientation of the GaAs wafer substrate.

4.2 Static MOKE measurements

Prior to our investigations, all samples which were provided to us had been characterized by measuring static MOKE hysteresis loops by using a continuous HeNe laser. The data of these measurements were helpful to identify hard and easy magneto-crystalline anisotropy axes as well as complementary information to the magnetization dynamics measured by means of TR-MOKE.

4.2.1 Single crystalline FeCo on GaAs

Fig. 4.1 shows hysteresis curves of sample As48 determined by MOKE. The square loop in Fig. 4.1(a) marks a single switching event of the magnetization in case of a field sweep along the $[110]$ crystal direction. By contrast, if the field sweep was performed along a direction perpendicular to the latter (i.e. $[1-10]$), then magnetization reversal proceeded via two jumps, accompanied by a linear slope in between the discontinuities (Fig. 4.1(b)).

These hysteresis curves can be explained for by assuming the presence of both a cubic anisotropy of bulk FeCo with easy axes along $\langle 110 \rangle$ directions and an additional uniaxial anisotropy with a $[110]$ easy axis in the plane of the magnetic film [17]. This superposition is illustrated with respect to crystallographic directions in Fig. 4.2. When no external field is applied within the film plane, the equilibrium magnetization will be directed either along $[110]$ or $[-1-10]$ where the easy axes of uniaxial and cubic anisotropy coincide and establish a global energy minimum. The directions $[1-10]$ and $[-110]$ constitute an intermediate easy axis, because they are "easy" on the one hand due to cubic anisotropy, but "hard" on the other hand due to uniaxial anisotropy.

Within this model, the discontinuities appearing in Fig. 4.1(b) can be explained as follows. If the external field \mathbf{B}_{ext} applied along an intermediate axis (e.g. $[1-10]$) is large enough, then \mathbf{M} will be forced to align parallel to \mathbf{B}_{ext} . When the field is decreased continuously, the force

4 Static Properties of the Samples

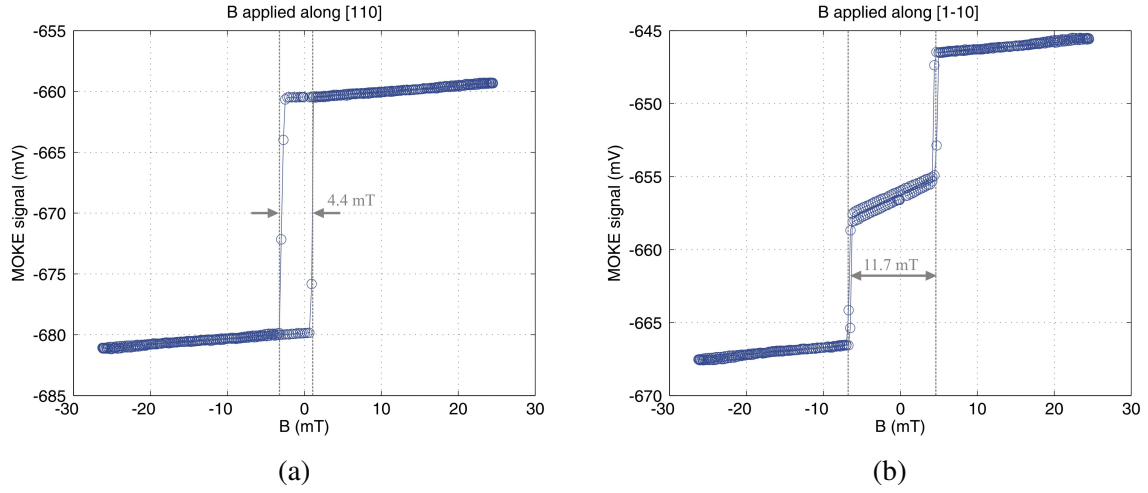


Figure 4.1: MOKE hysteresis loops of As48 at RT.

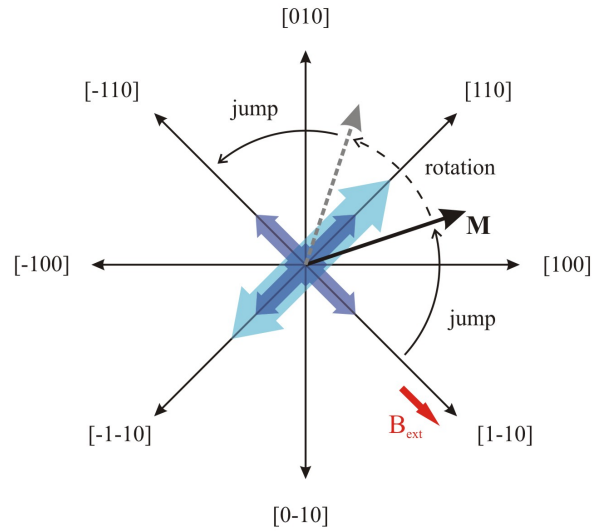


Figure 4.2: Schematic diagram of the easy directions of cubic anisotropy (dark blue arrows) and uniaxial anisotropy (bright blue arrows) as present in the investigated epitaxial FeCo film. As an example the evolution of the magnetization \mathbf{M} under the influence of a sweeping external field \mathbf{B}_{ext} applied along an intermediate axis is illustrated. The steps in the magnetization curve for a field sweep along $[1-10]$, as observed in the MOKE measurements of Fig.4.1(b), can be understood as evidence for a jump of \mathbf{M} towards (respectively away from) the easy axis when the anisotropy energy barrier has been overcome, while the linearly dependent part in the hysteresis curve describes a coherent rotation of \mathbf{M} .

which drags the magnetization towards the nearest easy axis will gain increasing influence until it finally overcomes the energy barrier which is constituted by the superposition of cubic and uniaxial anisotropies. At this point \mathbf{M} suddenly jumps to a new equilibrium direction close to the easy axis. This sudden change manifests itself as a step in the hysteresis curve as observed in Fig. 4.1(b). By further decreasing B_{ext} , the angle of the magnetization vector with respect to the easy axis gradually becomes smaller, reaching zero when $B_{ext} = 0$. \mathbf{M} continues its rotation for an increasing field of opposite sign, until it jumps over the "anisotropy energy barrier" again to align in parallel with B_{ext} .

4.2.2 Polycrystalline FeCo on GaAs

As the hysteresis curves show in Fig. 4.3, the [110] direction of the GaAs substrate was found to be an easy magnetization axis of the polycrystalline FeCo-sample (As40). It was surprising to find the presence of a uniaxial anisotropy. If one assumes that the FeCo-GaAs interface is responsible for the unidirectional behavior, then one might think that the Al interlayer could decouple the film from the GaAs. The static MOKE results prove that the situation is different.

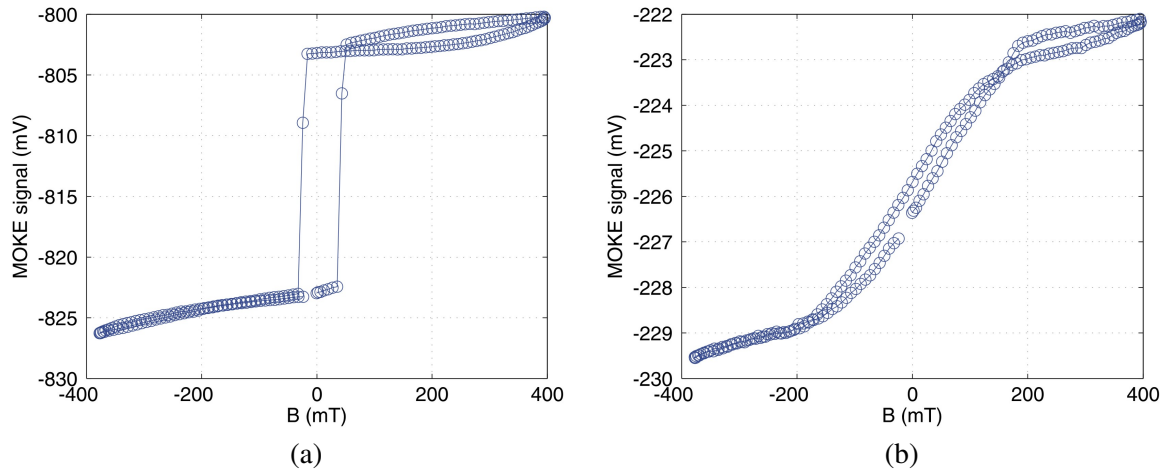


Figure 4.3: MOKE hysteresis loops of As40 at RT. The external field was swept along the [110] direction of the GaAs wafer in (a), respectively along [-110] in (b).

4.2.3 Single-crystalline Fe on GaAs

The MOKE measurements in Fig. 4.4 show that the sample As10 exhibited a pronounced easy magnetization axis along [110]. The presence of a cubic crystalline anisotropy was yet not apparent from the hysteresis curves. Although in case of the FeCo sample it was possible to sketch a magnetization reversal scheme just by using the MOKE data, it is not possible to make any further statements about the Fe sample without employing other investigation methods. However, since the magnetic properties of epitaxial Fe/GaAs(001) samples have been examined and reported before (e.g. in Refs. [18, 19]), we expected our sample As10 to be characterized

4 Static Properties of the Samples

by a superposition of a uniaxial anisotropy with the crystalline anisotropy of Fe as depicted in Fig. 4.5.

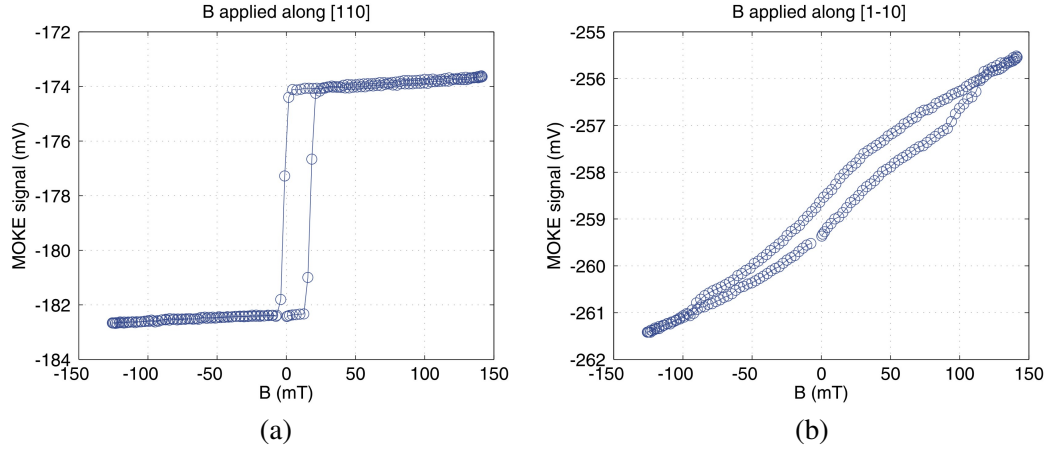


Figure 4.4: MOKE hysteresis loops of As10 at RT.

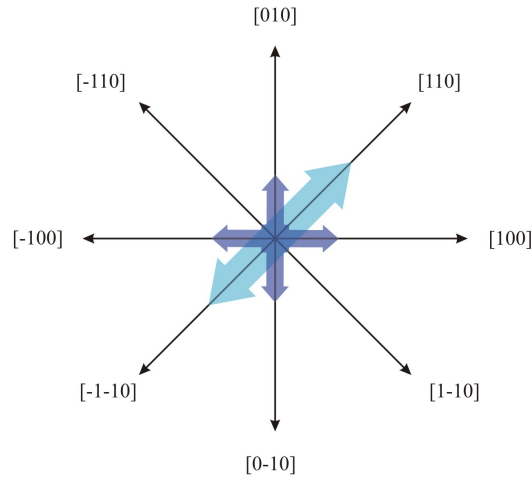


Figure 4.5: Diagram for the epitaxial Fe sample grown on GaAs(001), showing the easy magnetization directions of cubic anisotropy (dark blue) and the easy axis (bright blue) with respect to the lattice.

4.2.4 Polycrystalline Fe on GaAs

Similar to the polycrystalline FeCo on GaAs, the polycrystalline Fe sample showed a clear sign of a unidirectional magnetization behavior (Fig. 4.6). The Al interlayer did therefore not erase the uniaxial anisotropy which appears in case of direct growth of Fe on GaAs. Moreover, a MOKE curve which was taken by applying the external field at an angle of 45 degrees with

4 Static Properties of the Samples

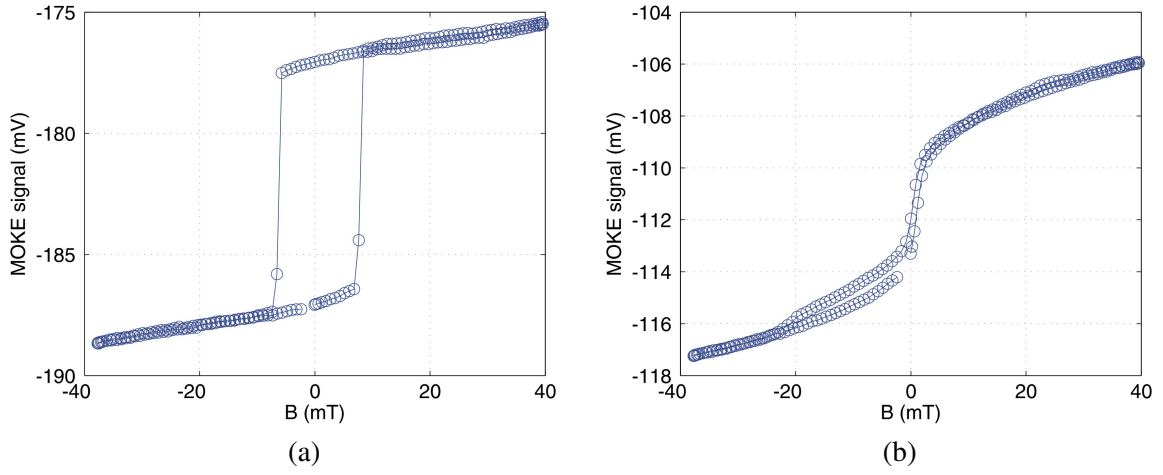


Figure 4.6: Hysteresis loops of As41 determined by MOKE at RT. The field was applied along the (a) [110] (b) [1-10] direction of the GaAs substrate crystal.

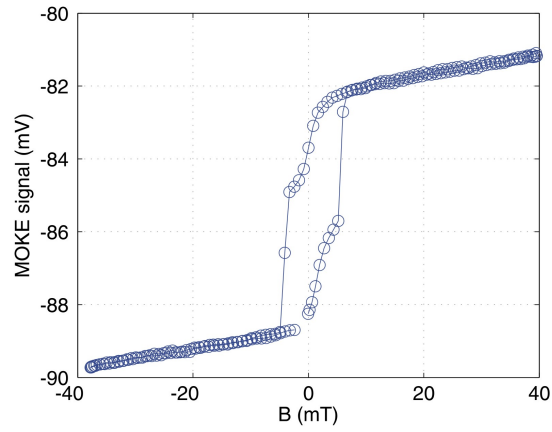


Figure 4.7: MOKE curve of sample As41. The field was applied at an angle of 45° with respect to the easy axis.

4 Static Properties of the Samples

respect to the easy magnetization axis. The discontinuities in the data curve of Fig. 4.7 reveal the presence of further anisotropies.

5 Results from TR-MOKE measurements

5.1 Single crystalline FeCo on GaAs(001)

The dynamic behavior of the magnetization in sample As48 was investigated at RT and at 10 K. We successfully conducted measurements of magnetization precession by means of photocurrent field pulse excitation. However, we were not able to detect a signal arising from the effect of an anisotropy field pulse. The results presented in the following focus on experiments carried out at RT by use of the former excitation mechanism.

A laser wavelength of 804 nm (which is above the GaAs band-gap excitation energy corresponding to ~ 870 nm at RT) was used for the utilization of photocurrent field pulses. The pump and probe fluencies were $5 \mu\text{J}/\text{cm}^2$ and $0.2 \mu\text{J}/\text{cm}^2$, respectively. In order to get an enhanced signal amplitude, the Schottky barrier was negatively biased to -2 V.¹ The laser-induced photocurrent was determined to be $\sim 24 \mu\text{A}$ per pump pulse, justifying a rough estimate (with the help of Ampère's law) of $480 \mu\text{T}$ maximum field strength for the photocurrent field pulse at a distance of $10 \mu\text{m}$ from the center of the pump beam focal spot.

5.1.1 Intermediate axis characteristics

Fig. 5.1 shows the results gained from TR-MOKE measurements at RT for \mathbf{B}_{ext} applied along [1-10]. The oscillation frequency behavior in Fig. 5.1(a) is symmetric for field sweeps in both directions, characterized by a large slope for $|\mathbf{B}_{ext}| \geq 6$ mT and a bump feature in the center. The run of these curves is attributed to the magnetic anisotropies intrinsic to the ferromagnetic film. It was suggested in 1947 by Kittel to treat magnetic anisotropies as equivalent to magnetic fields in their effect [8]. As already mentioned earlier in this text, the total field in which the magnetic moments precess is thus composed of the external field \mathbf{B}_{ext} and the anisotropy fields of the magnetic sample. Accordingly, at large \mathbf{B}_{ext} the precession frequency is approximately given by the Larmor formula $f = (2\pi)^{-1}\gamma |\mathbf{B}_{ext}|$, whereas at small \mathbf{B}_{ext} the anisotropy fields dominates the precessional dynamics.

Fig. 5.1(b) demonstrates the characteristics of the signal oscillation phase $\Delta\Phi$. Two phase jumps show up within a distance of 12.8 mT from each other, being well in accordance to the

¹It was shown in [1] that the amplitude of the oscillating out-of-plane component of the magnetization is affected by the bias voltage applied to the Schottky barrier. A negative voltage accelerates the motion of the photo-generated electron-hole pairs out of the depletion region and leads to an increased current in comparison to if no bias would be applied. Hence, a stronger tipping magnetic field is generated and the oscillation amplitude becomes enhanced with a negative bias.

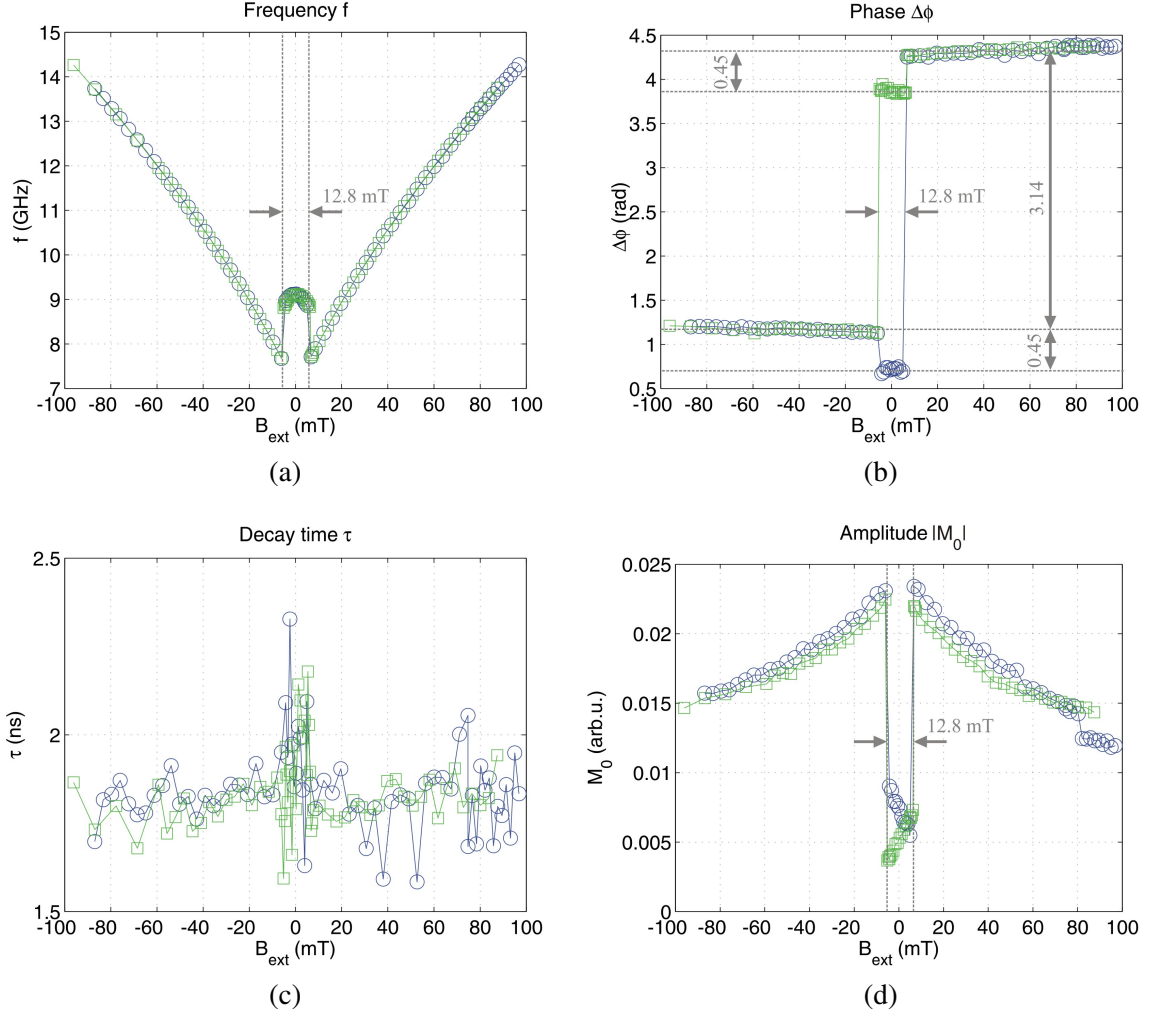


Figure 5.1: RT characteristics of the magnetization precession in the single-crystalline FeCo film measured as a function of external field B_{ext} , which was applied along the intermediate anisotropy direction [1-10]. The data of both the forward (negative to positive field, green data markers) and the reverse field sweep (blue data markers) are presented within the same graphs. The oscillation properties of the TR-MOKE signal are represented here by the values of (a) the precession frequency ω , (b) the oscillation phase $\Delta\Phi$, (c) decay time τ and (d) initial oscillation amplitude M_0 .

distance between the discontinuities in Fig. 4.1(b). A striking feature of the changes in $\Delta\Phi$ is the relative phase difference of π between $B_{ext} < 7$ mT and $B_{ext} > 7$ mT, as indicated in the figure. Such phase shifts appear due to the asymmetry established by a photocurrent field pulse, as reflected in the formation of two half planes with opposite sign in torque (Fig. 3.5 and Fig. 3.6) [1, 10].

The decay time of the oscillations remained relatively stable around an average of ~ 1.8 ns as a function of B_{ext} (Fig. 4.1(c)). The evolution of the initial amplitude M_0 in dependence of B_{ext} is presented in Fig. 5.1(d). It will be demonstrated in the following that the observed characteristics for M_0 as well as for $\Delta\Phi$ is comprehensible if one examines two-dimensional maps of the magnetization dynamics at specific fields.

Two-dimensional raster images of magnetization precession

By displacing the pump with respect to the probe beam focal spot stepwise and measuring the TR-MOKE signal amplitude at a fixed pump-probe delay successively, a limited area on the sample surface was rastered. The images of Fig. 5.2(a)-(d) show the resulting "maps" of the magnetization dynamics. The colors of the pixels represent the magnitude of the amplitude (see explanation below figure). Remarkably, the distance between the amplitude minima and maxima, being $\sim 20\mu\text{m}$, corresponds to the diameter of the pump beam on the sample surface. This confirms the assumption stated in Sec. 3.2.1 that the tipping field produced by the photocurrent should reach its highest value at the border of laser pulse spot.

Before capturing the image in Fig. 5.2(a), the external field had been continuously reduced from a high field (1 T) to 6.8 mT (which is just before the jumps in $\Delta\Phi$ and M_0). Fig. 5.2(b) shows an image after B_{ext} had been further decreased by a small amount to 6.6 mT. In comparison to (a), the excited regions had moved to new locations. Since B_{ext} had been applied along the intermediate axis, this event can be related to the switching of M_{eq} towards the easy axis. As the sweep of B_{ext} was continued and held at -5.3 mT, it was observed that the axis passing through the maxima of the excited regions had visibly turned by $\sim 10^\circ$. Then, after another tiny variation of B_{ext} from -5.3 mT to -5.5 mT, another switching of the latter axis was observed.

The images do not only reveal magnetization precession, but also the direction of equilibrium magnetization M_{eq} . Referring to Fig. 3.5(b), it is clear that the locations of largest amplitudes must be correlated with the positions where the torque given by $|M_{eq} \times H_{pulse}|$ is at a maximum; the torque, in turn, is strongest at the locations where the circular field lines of H_{pulse} intersect the equilibrium direction of the magnetic moments perpendicularly, i.e. the magnitude $|M_{eq} \times H_{pulse}|$ is maximized. Taking these correlations into account, one can deduce the orientation of M_{eq} from the images Fig. 5.2(a)-(d). This is visualized in Fig. 5.3 in the form of schematic drawings.

These observations can be put together with the measured dependencies of M_0 and $\Delta\Phi$ in order to attain an overall picture. The magnetization precession maps indicate a sudden jump of M_{eq} over the anisotropy barrier, followed by a coherent rotation and another jump. The characteristics of M_0 confirms these assumptions; since M_0 is related to the strength of the locally acting torque (at the position of the black dot in Fig. 5.2), a linear dependence of its value is evidence for a coherent rotation of M_{eq} . The distinctive discontinuities of M_0 , which

5 Results from TR-MOKE measurements

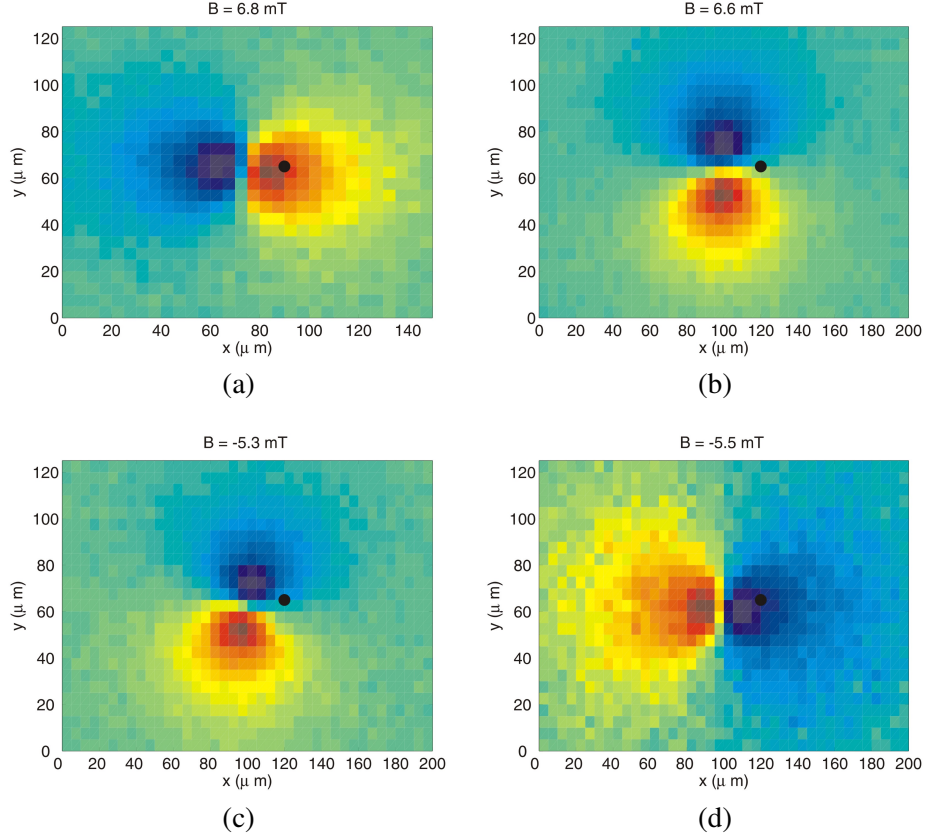


Figure 5.2: Maps showing the spatially resolved TR-MOKE signal amplitude, where areas of the ferromagnet with the magnetization being in a precessional state are visualized. \mathbf{B}_{ext} was swept parallel to the x-axis. The pump-probe delay was chosen such for the images that $M_z(t)$ was measured at a peak of its oscillation. The corresponding delays were 210 ps in (a), 175 ps in (b), 175 ps in (c) and 230 ps in (d). The intermediate axis ([1-10] resp. [-110]) was not exactly parallel to the x-axis, but slightly tilted. The colors in the images mark the magnitude and sign of the amplitude in the M_z -oscillations. Dark Red and dark blue mark regions of large oscillations, but of opposite sign in amplitude (and phase). Green is assigned to areas of no or vanishingly small oscillating signal. The black dot denotes the location on the sample surface at which the measurements presented in Fig. 5.1 were performed.

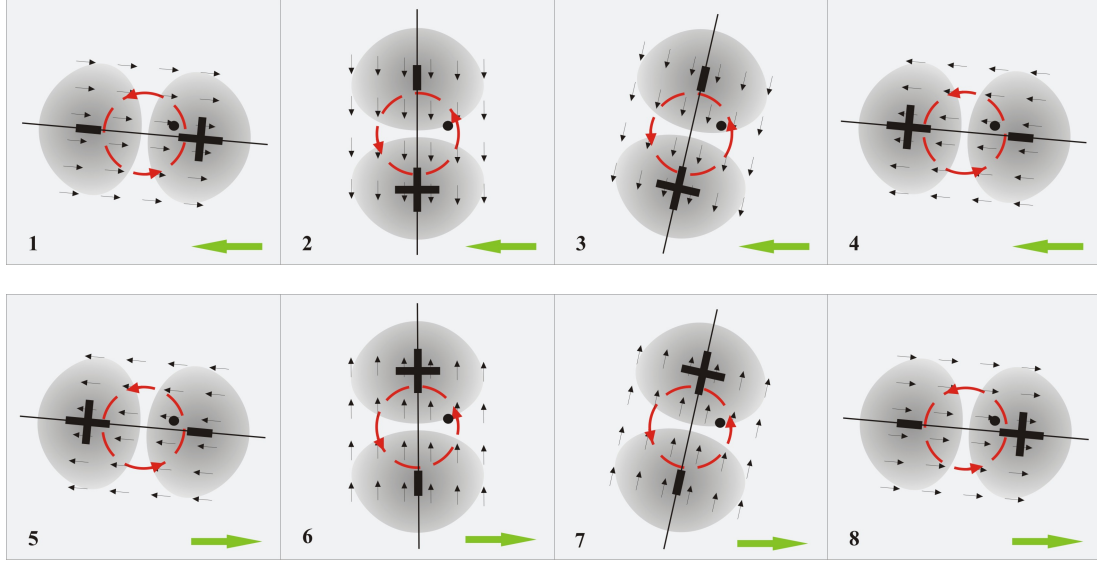


Figure 5.3: **1 to 4**: Schematic representations of the physical situations corresponding to the images (a) to (d) of Fig. 5.2. The green arrow denotes the direction along which \mathbf{B}_{ext} was swept. Again, the black dot marks the position at which the TR-MOKE signal was measured. At the points where the solid line (which denotes the direction of \mathbf{M}_{eq}) and the field lines of the circular magnetic field intersect perpendicularly, the precession-initiating torque is maximized. Note that the magnitude of the torque also depends on the distance to the center of the circular magnetic field (described in Sec. 3.2.1). During a field sweep in the opposite direction, the switching behavior is assumed to occur as depicted in the images **5 to 8**.

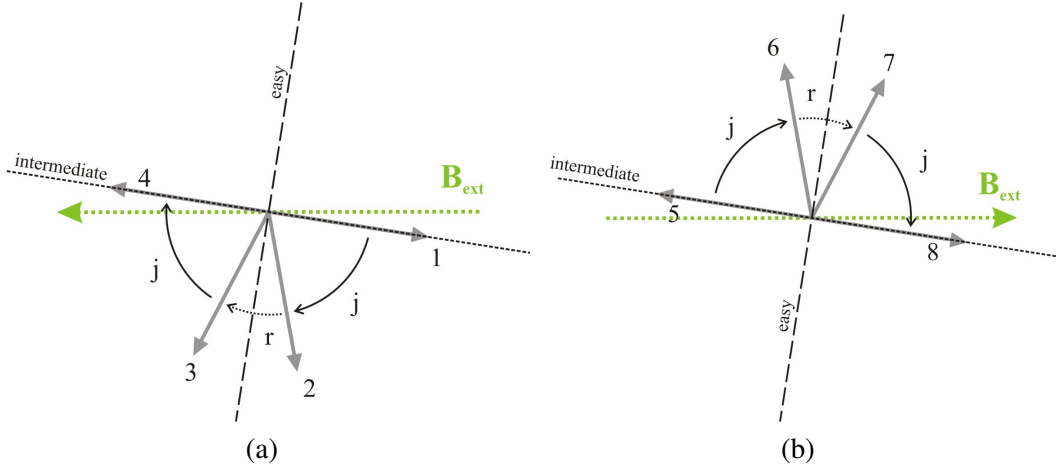


Figure 5.4: (a) and (b): Depiction of the orientations of \mathbf{M}_{eq} (arrows 1 to 4 and 5 to 8, respectively) corresponding to Fig. 5.3. j=jump, r=rotation. In (a), \mathbf{B}_{ext} is swept from positive to negative values, whereas (b) shows the opposite case. When \mathbf{M}_{eq} is at position 1, \mathbf{B}_{ext} is just large enough to avoid a switching towards the easy axis. After a slight decrease of \mathbf{B}_{ext} , \mathbf{M}_{eq} jumps over the anisotropy barrier towards a direction nearest to the easy axis (position 2). Subsequently, \mathbf{M}_{eq} rotates as a function of \mathbf{B}_{ext} (position 2 to 3). Then, \mathbf{M}_{eq} jumps again (position 3 to 4) after a slight increase of \mathbf{B}_{ext} . The same processes happen equivalently in (b); however, the switching behavior of \mathbf{M}_{eq} is not simply reverted, but occurs from above (i.e. clockwise).

are 12.8 mT apart from each other, reveal the jumps over the anisotropy barrier. These events are in accordance with the MOKE hysteresis curve in Fig. 4.1(b), where the steps were 11.7 mT apart.

The schematic drawings in Fig. 5.3 and in Fig. 5.4 should facilitate understanding the linear dependence of M_0 . In particular, Fig. 5.4 (1)-(4) draw the situation for the case where \mathbf{B}_{ext} is swept from positive to negative field values. Referring to the position of the black dot in the drawings, the transition from image (1) to (2) is specified by a switching of the direction of the torque and accordingly the phase. We stated before that the transition from the images (2) to (3) is characterized by a coherent rotation of \mathbf{M}_{eq} , therefore the rotation should result in a linear increase in the local torque. This is revealed in the behavior of M_0 (Fig. 5.1(d)). In the other case where \mathbf{B}_{ext} is swept in the opposite direction (Fig. 5.4 (5)-(8)), the same processes reoccur as in (1)-(4), but the magnetization reversal proceeds over the upper half plane (Fig. 5.4).

At first sight, the behavior of M_0 for fields larger than ± 7 mT seems surprising, because it does not fit in the picture described above. From the illustrations given in Fig. 5.4, one would expect the magnetization to gradually align parallel to the direction of \mathbf{B}_{ext} , if the field is increased to higher magnitudes. This should be accompanied by a rise in M_0 , as for example the drawing Fig. 5.4 (1) would suggest; the black dot would approach the line of maximum torque. Instead, the initial precession amplitude M_0 continues to decline even if the field is increased up to 1 T (Fig. 5.5).

5 Results from TR-MOKE measurements

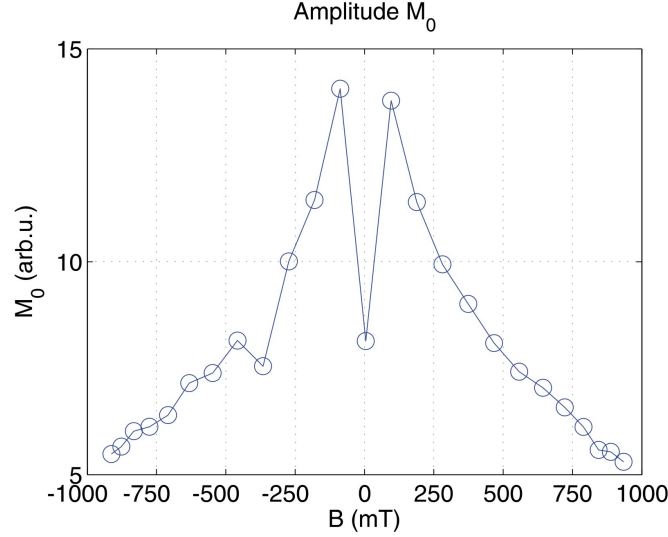


Figure 5.5: Behavior of M_0 for a sweep of \mathbf{B}_{ext} over a large interval.

This suppression effect of a high magnetic field upon M_0 is rather curious. In an attempt to find an explanation for this finding, we developed the following "naive" approach to the problem which makes use of energy considerations. By neglecting cubic crystal anisotropy terms, we can formulate the expression

$$E = - \underbrace{M_s B_y \sin \theta \sin(\phi)}_{\text{Zeeman}} + \underbrace{K_u \sin^2 \theta \sin^2(\phi)}_{\text{Uniaxial anisotropy}} + \underbrace{\frac{1}{2} \mu_0 M_{eff} M_s \cos^2 \theta}_{\text{Shape anisotropy}} \quad (5.1)$$

for the total magnetic energy. Here, θ and ϕ designate the polar and the azimuthal angle which define the spatial position of the magnetization vector. ϕ is counted from the x-axis of the cartesian coordinate system. The Zeeman term therefore characterizes the y axis as the hard magnetization axis, provided that K_u is positive. B_y designates an external field which is acting along the y-axis.

The equation Equ. (5.1) defines an energy landscape for the spatial orientation magnetization vector. Its energy minimum can be changed by varying the external field. If the magnitude of B_y is increased, it will gain increasing influence in the total energy; the magnetization vector \mathbf{M} will finally align in parallel with the y-axis if B_y becomes large enough. A further rise of B_y will lead to the development of a pronounced energy minimum within the energy landscape of \mathbf{M} , making other orientations of \mathbf{M} than a parallel alignment to B_y even more unfavorable. Therefore, it will become more and more difficult to tip the magnetization vector away from that direction. Consequently, as a function of increasing external magnetic field, the photocurrent field pulse - which initiates magnetization precession - will lose effect in exciting the magnetic moments out of their equilibrium orientation, because the magnetic moments will become more and more "rigid". These arguments might explain the fact that M_0 - which is related to the factor by which the magnetic moments are tipped away from equilibrium - decreases as a function of external field. However, our explanation is admittedly not well-founded, but deduced from simple consideration.

5.1.2 Easy axis characteristics

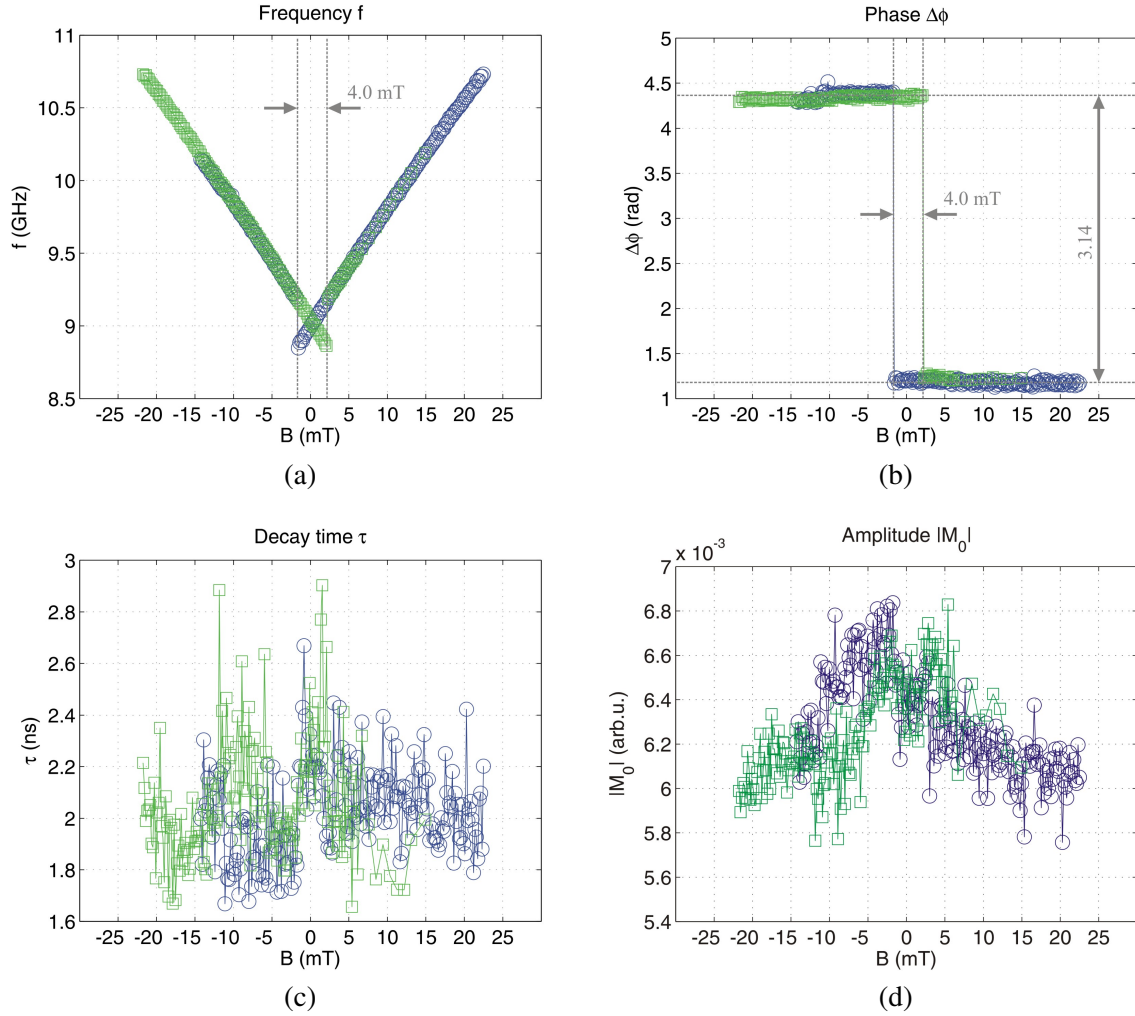


Figure 5.6: TR-MOKE signal characteristics of As48 measured at RT. Here \mathbf{B}_{ext} was swept along the easy axis direction [110] (negative to positive field - \rightarrow green data markers, reverse - \leftarrow blue data markers).

The characteristics of the dynamic parameters for field sweeps along the [110] direction differed from those of the intermediate axis, as can be seen from Fig. 5.1.2. The frequency shows a linear monotonic dependence from the field (Fig. 5.1.2(a)), with a discontinuity appearing at a field value of 2 mT during the forward field sweep (respectively at -2 mT during the reverse field sweep). The phase reacts at exactly the same remanence field as ω with a jump of the amount of π , while it remains uninfluenced at other field values (Fig. 5.1.2(b)). These characteristics are in accordance to the switching behavior of the magnetization in the MOKE hysteresis loop Fig. 4.1(a), as one can verify by comparing the designated opening values. Contrary to the observations of the measurements where \mathbf{B}_{ext} was swept along the intermediate axis, the amplitude of the oscillations did not show significant jumps. This result

is not surprising, in fact it proves that the amplitude (and therefore the local strength of the precession-initiating torque acting upon the magnetic moments) is independent of a parallel or antiparallel orientation of the magnetization to the easy axis. Although the magnitude of M_0 was unaffected by the magnetization switching, the jump of π in the oscillation phase proves that the direction of the locally acting torque had been reversed. Again, in simple terms: if the magnetic moments were being tipped upwards from the sample plane before, then after the switching of M_{eq} they were excited downwards from the sample plane.

5.1.3 Numerical fits

By using the expression Equ. (2.16) for the total magnetic energy and following the procedure described in Sec. 3.3.2, numerical fits to the measured precession frequency data were performed. As Fig. 5.7(a) and (b) show, the fits match extraordinary well with the measurement data. These results demonstrate the high accuracy of the model for the total magnetic energy of the system. Our fitting technique did not only enable us to calculate the frequency characteristics, but also to determine the trajectory of the magnetization vector M_{eq} as a function of B_{ext} (Fig. 5.8).²

The evaluated values for the anisotropy constants are presented in Tab. 5.1. K_2 is not listed, because it was found that the fits were not sensitive to this higher-order anisotropy constant. As one can see, there is only a slight deviation between the values of the intermediate axis field sweep and the easy axis field sweep. By taking the mean values of each K_1 and K_u and multiplying them by the saturation magnetization for $\text{Fe}_{30}\text{Co}_{70}$, which amounts $\mu_0 M_s \approx 2.25$ T [20], we determined the anisotropy constants as $K_u = 9.83$ kJ/m³ and $K_1 = -38.27$ kJ/m³. In search for comparable values for the anisotropy constants, we found in [21] that the bulk value of K_1 in case of $\text{Fe}_{34}\text{Co}_{66}$ amounts -38 kJ/m³. This value corresponds very well to our calculated value.

For the special case of epitaxial FeCo film samples on GaAs(001), K_u and K_1 can also be determined from the static MOKE measurements just by specifying the value for the so-called "split field", which amount 11.7 mT for our sample (see Fig. 4.1), and the magnitude for the linear slope [17]. By this means, the anisotropy constants had been determined as $K_u = 9.87$ kJ/m³ and $K_1 = -36.12$ kJ/m³ at RT [22]. The remarkably well accordance of these values to the fitting results reassured us that that our fitting technique provided reliable results for the anisotropy constant.

Field sweep direction	$\frac{K_u}{\mu_0 M_s} [\frac{\text{kA}}{\text{m}}]$	$\frac{K_1}{\mu_0 M_s} [\frac{\text{kA}}{\text{m}}]$	$M_{eff} [\frac{\text{kA}}{\text{m}}]$
Intermediate axis	4.57	-17.21	1552.94
Easy axis	4.17	-16.81	1558.50

Table 5.1: List of anisotropy constants, as extracted from numerical fits.

²Note that the evaluation of the equilibrium orientation of the magnetization was one of the steps in our fitting routine (Sec. 3.3.2). The trajectory of the magnetization vector could thus be reconstructed.

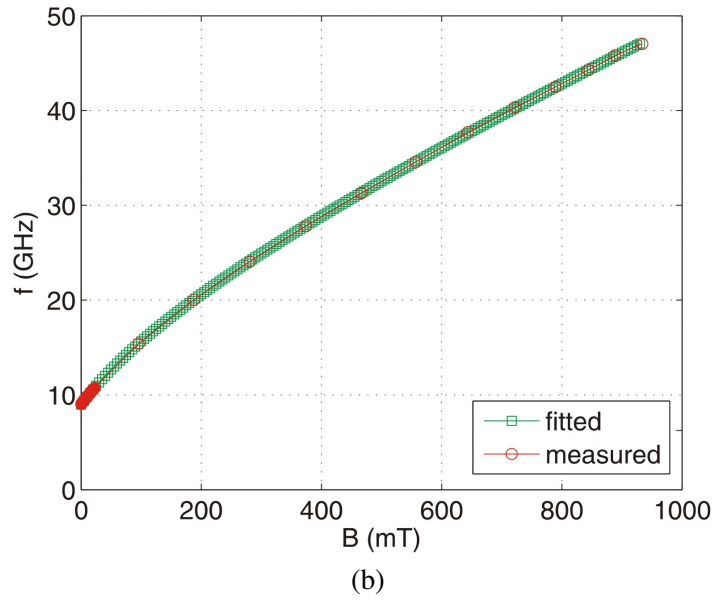
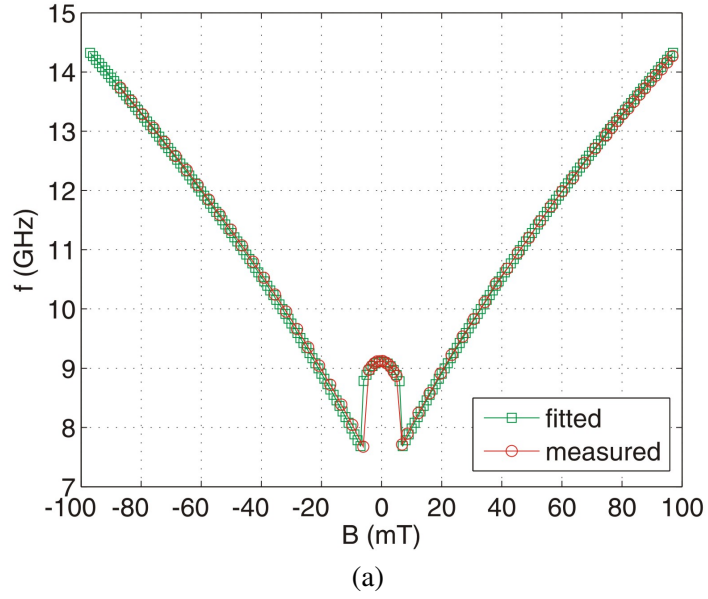


Figure 5.7: Measurement data of the frequency characteristics and corresponding fitting curves for **(a)** B_{ext} swept along the intermediate axis **(b)** B_{ext} swept along the easy axis.

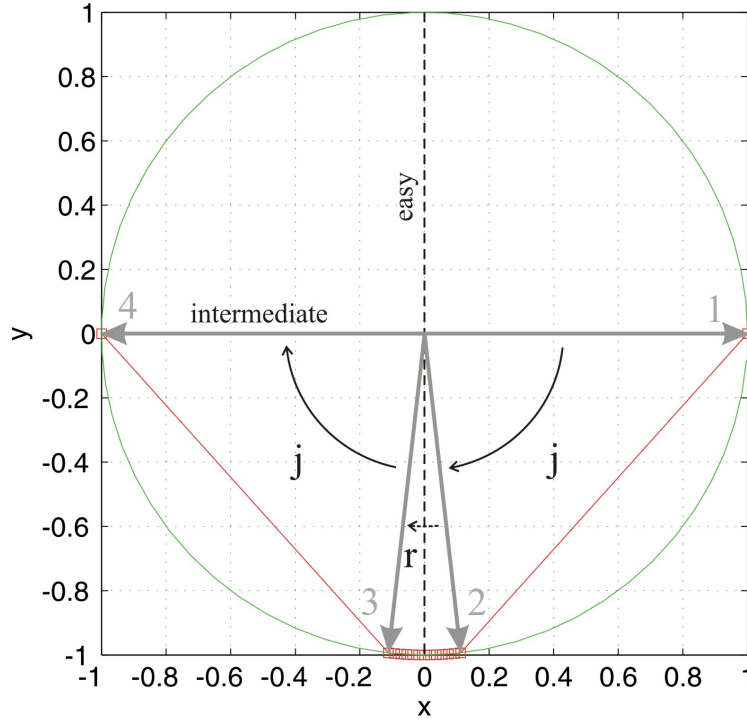


Figure 5.8: Calculated trajectory (red data markers) of the magnetization vector for a simulated field sweep from 100 mT to -100 mT in steps of 1 mT. x and y denote directions within the sample plane. The sequence of the four specific orientations of the magnetization vector (grey arrow) before/after the jumps over the anisotropy barrier is designated by the numbers 1-4. This trajectory is in fact consistent with the stated jumps (j) and rotations (r) of \mathbf{M}_{eq} as observed in the raster images Fig. 5.2. The green circle describes the unit circle defined by \mathbf{M}_{eq}/M_s .

5.2 Polycrystalline FeCo

In a subsequent step, we measured the precessional magnetization characteristics in the polycrystalline FeCo sample (As40). Static MOKE measurements had revealed the presence of a uniaxial anisotropy. As can be seen in Fig. 5.9, the curvature of the precession frequency spectrum deviated significantly from what we had observed in the epitaxial FeCo film.

From the numerical fit, we obtained $K_u/\mu_0 M_s = 0.54 \text{ kA/m}$, $K_1/\mu_0 M_s = 3.75 \text{ kA/m}$ and $M_{eff} = 1216.063 \text{ kA/m}$. Again using $\mu_0 M_s \approx 2.25 \text{ T}$, these values corresponds to $K_u = 1.21 \text{ kJ/m}^3$ and $K_1 = 8.44 \text{ kJ/m}^3$. K_u is ~ 8 times smaller than the value for As48, proving that the Al interlayer between the substrate and the film diminishes the uniaxial behavior. The finding that K_1 is positive is remarkable; this means that the $\langle 100 \rangle$ directions are the hard axes of cubic anisotropy in this sample. In contrast, the $\langle 100 \rangle$ directions were the easy axes of cubic anisotropy in the epitaxial FeCo sample (due to the positive sign of K_1).

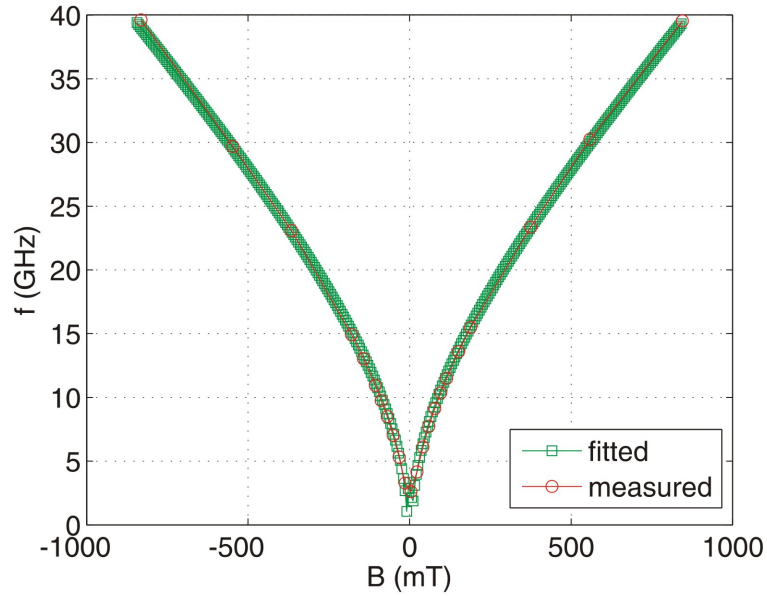


Figure 5.9: Graph showing data of the magnetization precession frequency (as observed at RT in sample As40) together with its fitting curve. The field was swept (approximately) along the $[110]$ direction of the GaAs substrate, which had been determined as the easy axis from static MOKE measurements.

5.3 Single crystalline Fe on GaAs(001)

The epitaxial Fe/GaAs(001) sample was investigated at low temperatures as well as at RT. Typically, a bias voltage of -2V was applied to the sample. The pump and probe fluencies were again $5 \mu\text{J}/\text{cm}^2$ and $0.2 \mu\text{J}/\text{cm}^2$. All measurements were performed with an external field applied along the hard axis of the sample (i.e. [1-10] direction, see Fig. 4.4).

5.3.1 Low temperature characteristics

Our TR-MOKE measurements at 10 and 20 K of the As10 sample provided us with intriguing results. Using photocurrent field pulses, we were able to detect the curious characteristics of $\Delta\Phi$, M_0 and τ , which differed markedly from the results gained from the As48 sample. Unexpectedly, we also successfully employed the anisotropy field pulse with a laser wavelength of 850 nm, which was below the bandgap excitation energy of GaAs. It was rather surprising that it was possible to observe magnetization precession induced by the latter excitation mechanism in this case, since the pump pulse fluencies in our experiments amounted to $5 \mu\text{J}/\text{cm}^2$, whereas the typical values reported were at least by a factor of 10^3 times larger [11, 12, 23]. Moreover, we could observe an anisotropy-change-induced effect only in the experiments which we conducted at 10 and 20 K. At RT, there was no sign whatsoever of magnetization precession detectable in the TR-MOKE signal.

Excitation via photocurrent field pulse

A laser wavelength of 805 nm was used in order to generate photocurrent field pulses. Fig. 5.10 shows the measured precession characteristics as a function of external magnetic field at 10 K. The frequency spectrum was quite different compared to the epitaxial FeCo sample. That was to be expected, as the two samples (As10 and As48) exhibited distinct magnetic anisotropies.

Strangely, three distinctive phase changes were observed which could not be associated with features of the static MOKE measurements. The exact reason for this finding is not clear, but presumably the characteristics of the phase reflects the reversal behavior of the magnetization. As further measurements were conducted where the field was swept in finer steps, a smooth transition in the phase revealed itself (Fig. 5.11). This is a quite striking feature; furthermore, the phase difference of π between -20 mT and 30 mT attracts attention. We could not explain why a smooth transition of the precession phase should occur.

The events of the phase changes were obviously accompanied by characteristic features in decay time and oscillation amplitude. A remarkable feature in M_0 is the pronounced peak at ~ 140 mT. τ was between 3 to 10 times smaller than the value of the FeCo sample at RT.

5 Results from TR-MOKE measurements

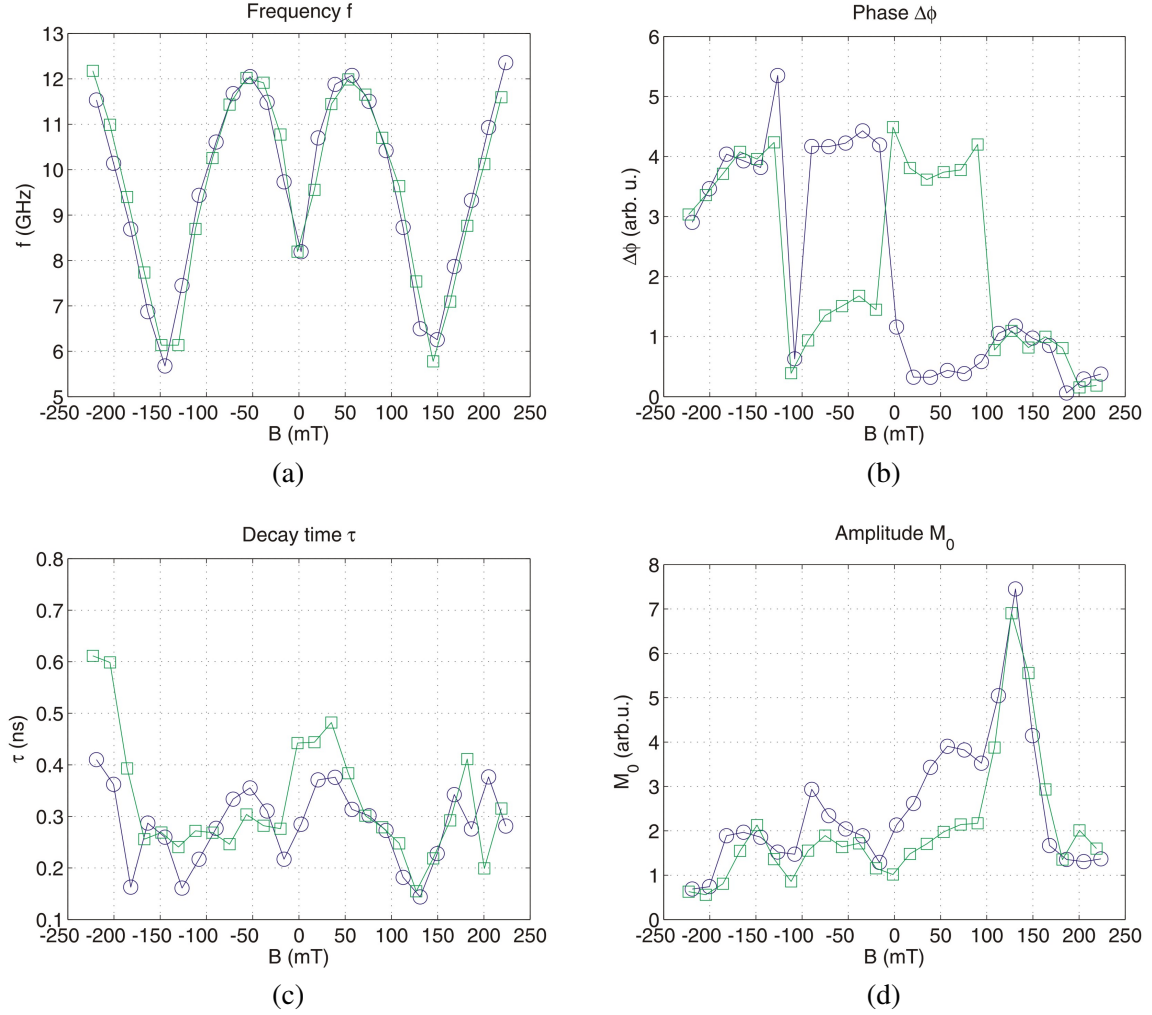


Figure 5.10: Precession characteristics of As10 at 10 K. Green squares mark the data of the forward field sweep (negative to positive field values), blue circles denote the reverse field sweep measurements.

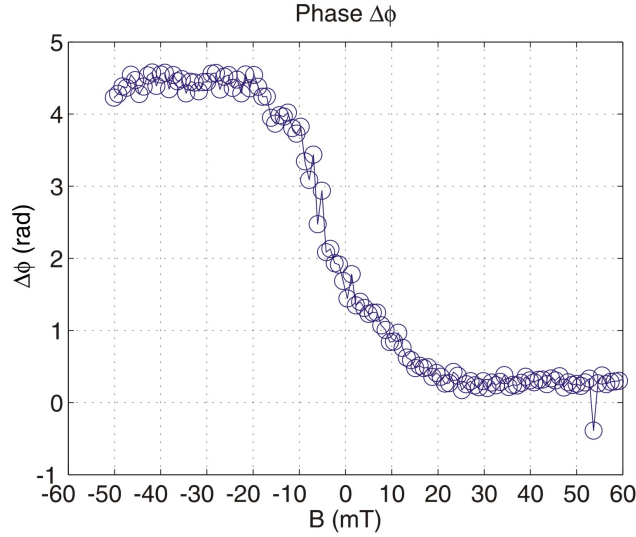


Figure 5.11: Surprisingly, the phase change shown in Fig. 5.10(b) was not abrupt. Instead, $\Delta\Phi$ experienced a smooth transition by an amount of π .

Excitation via anisotropy field pulse

The measurement results presented in Fig. 5.12 were gained at 20 K by using a laser wavelength of 850 nm, which is below the bandgap excitation energy. It should be noted that it was tricky to detect the signal, because it was almost vanishingly small. The frequency spectrum had the same curvature as it was observed in Fig. 5.10, demonstrating that magnetization precession initiated by an anisotropy field pulse proceeds in an analogous manner as in case of a photocurrent field pulse excitation.

The most noticeable features of the precession characteristics are the intriguing jumps in $\Delta\Phi$ by the amount of π . This phase behavior was in fact reproducible in further conducted measurements. We could not find any possible explanation for this intriguing finding. Anyhow, it is obvious from the measurement data that the nature of the phase changes is not the same as in photocurrent field pulse-initiated magnetization precession.

Another notable feature is the dependence of M_0 upon the magnitude of the external field, which differs clearly from the behavior observed by the photocurrent field pulse excitation. However, the decay time τ is of similar magnitude.

5 Results from TR-MOKE measurements

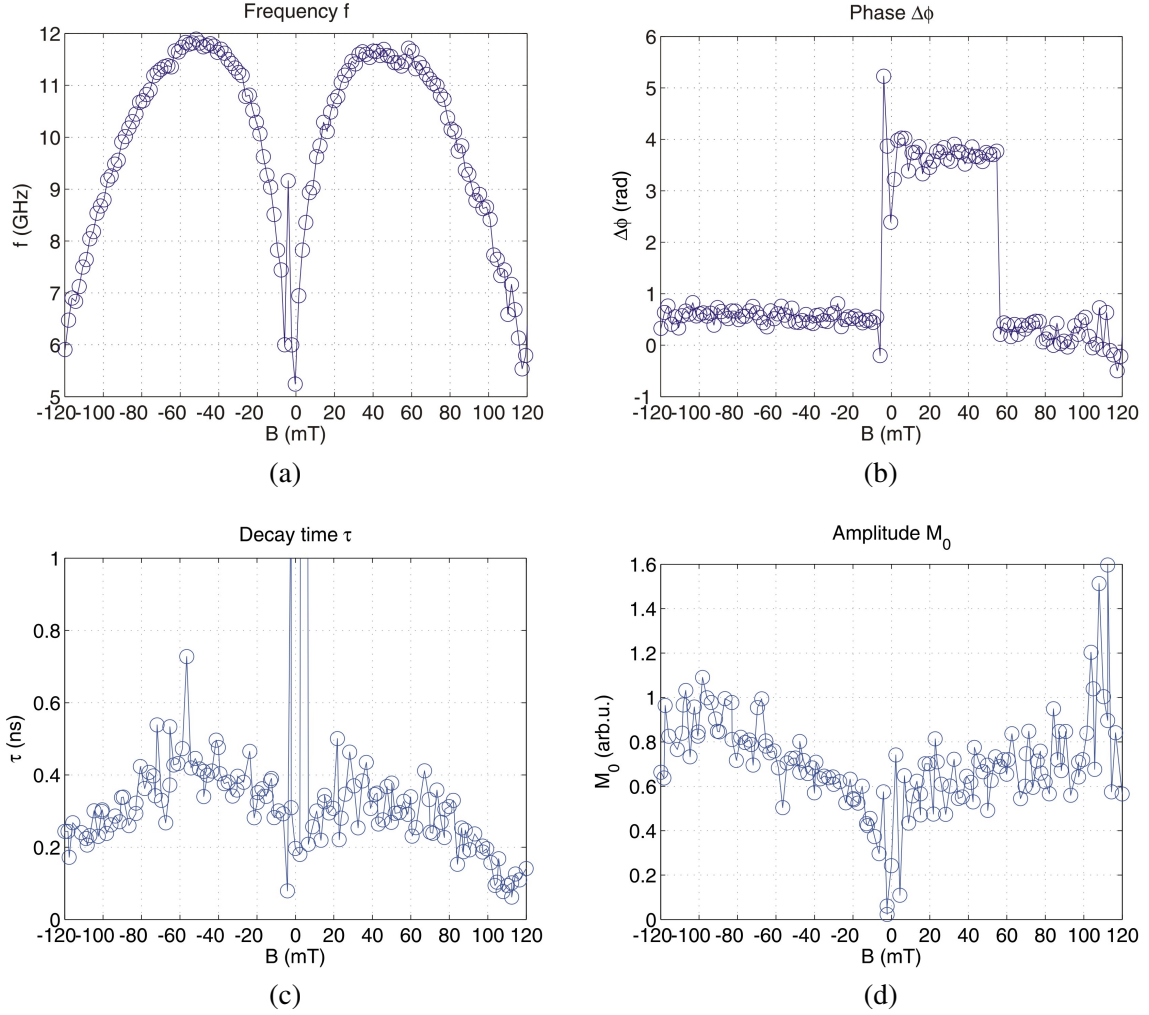


Figure 5.12: Characteristics of anisotropy field pulse-induced precession as observed in sample As10 at 20 K. The external field was swept from negative to positive values. The sweep in the opposite direction (not shown in the graphs) lead to a reversal of the jump positions in $\Delta\Phi$.

5.3.2 Numerical fits

The effect of varying the temperature of the sample is demonstrated in Fig. 5.13, where the different frequency characteristics are shown. As one can see there, the w-shaped curvature broadens with decreasing temperature. In order to find out how this observance can be related to the anisotropies, we fitted the curves and extracted the parameters K_1, K_u and M_{eff} . The results are summarized in Tab. 5.2. The computed curve for the 10 K measurement is shown as an example in Fig. 5.14 together with the measurement data in order to demonstrate the accuracy of the fit.

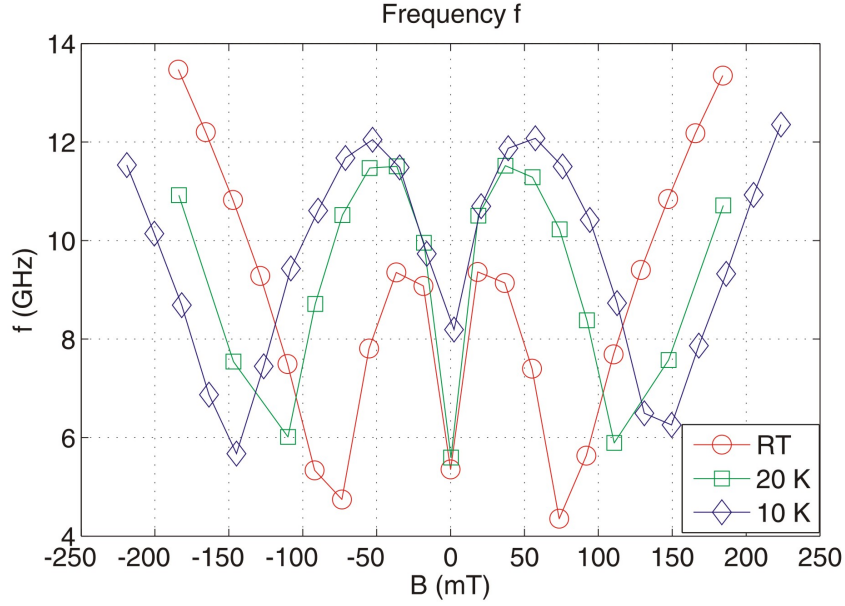


Figure 5.13: Frequency spectra at 10 K, 20 K and RT.

Using the value $\mu_0 M_s = 2.1451$ T for the bulk saturation magnetization of Fe [24], we obtained $K_1 = 35.89 \text{ kJ/m}^3$ and $K_u = 27.99 \text{ kJ/m}^3$ from the RT measurements. In comparison, bulk Fe is characterized by $K_1 = 48 \text{ kJ/m}^3$ [24].

Temperature	$\frac{K_u}{\mu_0 M_s} \left[\frac{\text{kA}}{\text{m}} \right]$	$\frac{K_1}{\mu_0 M_s} \left[\frac{\text{kA}}{\text{m}} \right]$	$M_{eff} \left[\frac{\text{kA}}{\text{m}} \right]$
RT	13.05	16.73	1491.63
20 K	26.69	18.66	1606.07
10 K	35.40	19.25	1428.19

Table 5.2: Temperature dependence of the anisotropy constants, as evaluated from fits to the frequency curves of sample As10.

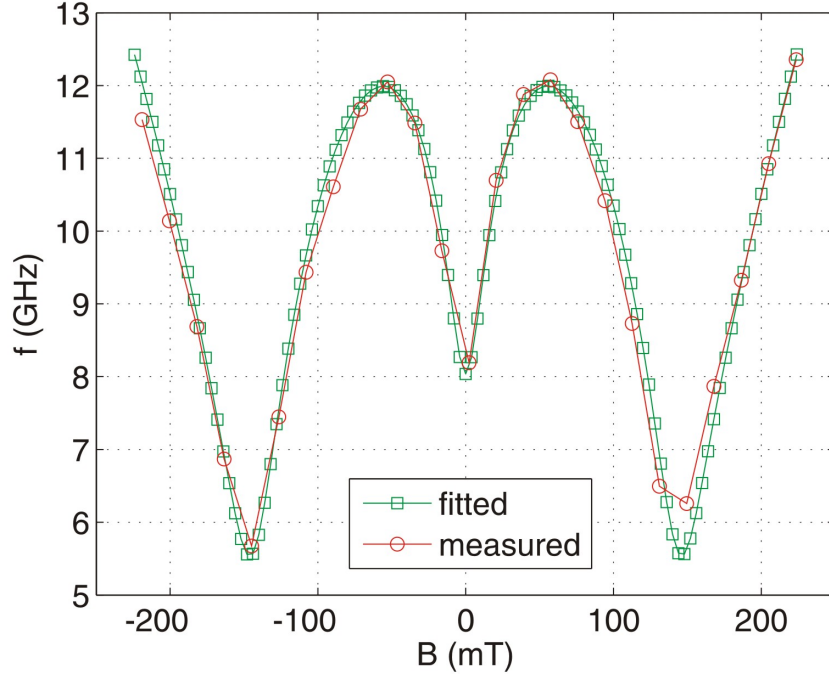
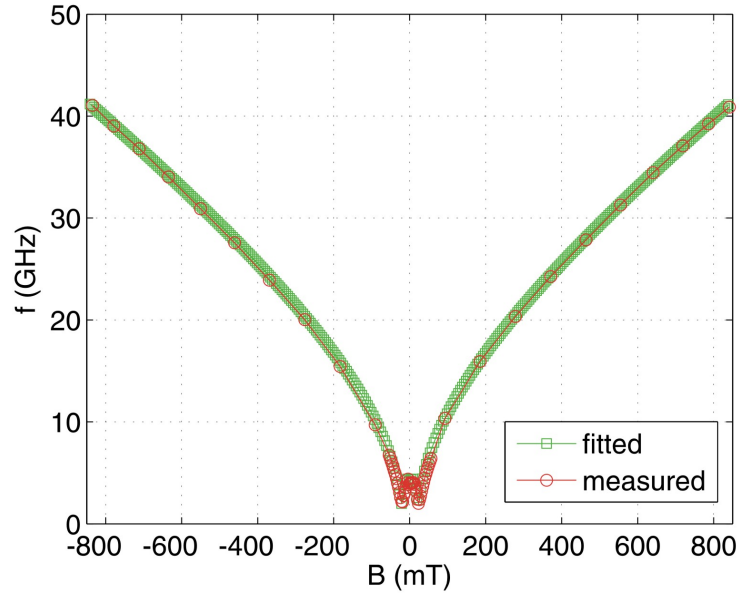


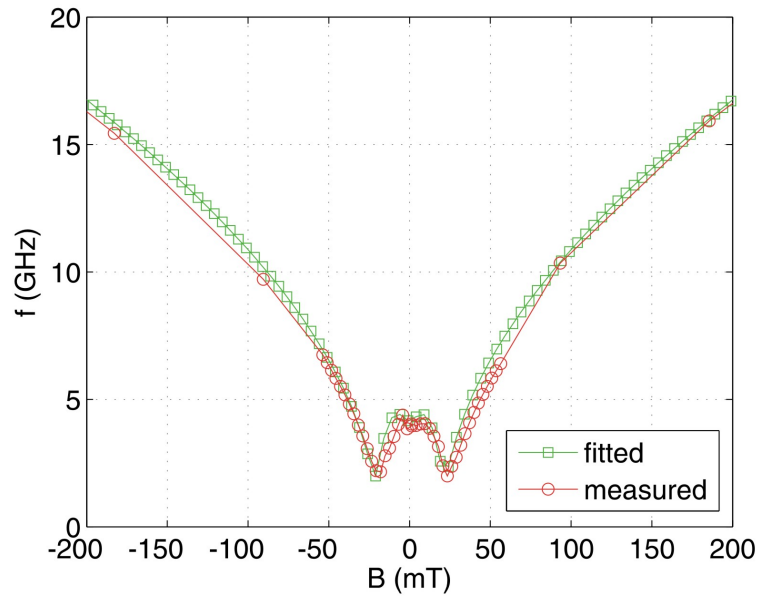
Figure 5.14: Measurement data and fitting curve for the precession frequency spectrum at 10 K.

5.4 Polycrystalline Fe

Fig. 5.15 shows the frequency spectrum of the polycrystalline Fe sample at room temperature. It was found from the fitting results that $K_u = 6.50$ kA/m, $K_1 = 1.64$ kA/m and $M_{eff} = 1425.92$ kA/m. As in the polycrystalline FeCo sample, K_u had been diminished by the Al interlayer between the film and the GaAs substrate. K_1 was found to be smaller by a factor of ~ 10 in comparison to the epitaxial Fe sample. Expressed in kJ/m³, K_u and K_1 amount 13.95 and 3.5.



(a)



(b)

Figure 5.15: Precession frequency spectrum of sample As41 for a field applied along the hard axis of the film. In (a), the overall characteristics is shown. In order to demonstrate the accurateness of the fit, a zoom to the data as is shown in (b).

6 Summary and Outlook

In the course of this thesis, optical pump-probe experiments with laser pulses of 3 ps length were carried out in order to study ultrafast magnetization dynamics in thin both epitaxial and polycrystalline Fe and FeCo films grown on GaAs (001). By adjusting the laser to a wavelength which gave rise to the generation of a transient photocurrent across the Schottky barrier upon the incidence of a pump pulse, an in-plane magnetic field pulse was generated which initiated the coherent precession of the magnetization. The time-resolved evolution of the magnetization component perpendicular to the sample surface was detected by varying the delay between the pump and the probe pulses.

In order to examine the characteristics of the precession, an external magnetic field was applied in the plane of the film and its magnitude was swept. The magnetization dynamics was successively measured for each field value. The corresponding characteristics of the precession reflected the magnetic properties of the samples.

Some interesting features of the precessional behavior in the epitaxial FeCo sample were discovered. The phase and the amplitude of the precession were found to change abruptly at transition fields which corresponded to jumps observed in hysteresis loops. Hence, these discontinuities were correlated to events where the magnetization had switched to a new equilibrium direction. Two-dimensional scanning images of the momentary magnetic state in the surrounding area where the pump pulses had impinged further clarified the measured dependencies. On the basis of the data, the characteristics of the precession amplitude and phase were explained. In particular, it was elucidated how the phase changes of the amount of π and the linear dependence of the amplitude upon variations of the external magnetic field within a small interval around zero field came about. However, the discovery that the amplitude is increasingly suppressed with higher external field magnitudes should be further investigated, because it was not sufficiently understood. It should be examined whether this suppression effect was unique for that specific sample or if it appears in other ferromagnetic materials.

The epitaxial Fe sample provided some intriguing results. First of all, it was the only sample where we observed magnetization precession initiated by an "anisotropy field pulse". The latter was realized with a laser wavelength below the bandgap excitation energy, so that it was not the generation of a photocurrent which gave rise to the perturbation of the magnetic moments, but a sudden change of the magnetic anisotropies induced by the heat transferred to the lattice by a pump pulse. Especially the phase behavior as a function of external magnetic field was striking, since it exhibited two jumps by the amount of π at specific field values and was determined to be constant otherwise. Possible reasons for the occurrence of such phase changes remain to be found. However, the magnetic field dependence of the frequency was shown to be equivalent to the case where the photocurrent generation across the Schottky junction had been exploited to launch a precession. In addition, measurements of the precessional characteristics where the latter excitation mechanism had been employed revealed an intriguing behavior of the

6 *Summary and Outlook*

precession phase. Curiously, the phase experienced a smooth transition when the external field was varied from positive to negative values. Further measurements of magnetization precession in similar samples might help to find answers to the open questions concerning the phase characteristics.

From numerical fits to the observed frequency data, the magnetic anisotropy constants were evaluated for each sample. Their values were shown to increase in case of the epitaxial Fe sample when the temperature was lowered. A comparison of the epitaxial and the polycrystalline samples (both Fe and FeCo) showed that the polycrystalline films were characterized by diminished values for the uniaxial and the cubic crystalline anisotropy constants.

7 Acknowledgments

This diploma thesis was carried out at the research laboratories of IBM in Rüschlikon, Switzerland. At this point, I want to mention that I enjoyed it very much to work in the friendly working climate of the "Physics of the Nanoscale" group. I also want to acknowledge the support from the following people of the group:

- First of all, I want to thank Gian Salis very much for his great support. As my supervisor at IBM, he essentially contributed to the outcome of this work by his committed assistance. It was not only enjoyable working with him, but also very instructive and motivating.
- Rolf Allenspach, the head of "Physics of the Nanoscale", gave me the opportunity to conduct my thesis in his group. I am very grateful for his confidence and patience. It was owing to his insightful lecture that I developed a distinct interest in the exciting field of magnetism.
- I want to thank Santos Alvarado and Patrick Bouchon for the very good collaboration. They provided the high quality samples which were fundamental for the investigations, together with the static MOKE data.
- During my first weeks in the lab, Matthias Studer assisted me to cope with experimental issues. I am thankful for his friendly support.

I also want to express my gratitude to Silke Bühler-Paschen, my supervising Professor at UT Vienna. It was very kind of her to agree on the supervision of my diploma thesis.

Bibliography

- [1] Y. Acremann, M. Buess, C. H. Back, M. Dumm, G. Bayreuther, and D. Pescia, “Ultrafast generation of magnetic fields in a schottky diode,” *Nature*, vol. 414, p. 51, 2001.
- [2] M. van Kampen, C. Jozsa, J. T. Kohlhepp, P. LeClair, L. Lagae, W. J. M. de Jonge, and B. Koopmans, “All-optical probe of coherent spin waves,” *Phys. Rev. Lett.*, vol. 88, p. 227201, 2002.
- [3] S. Blundell, *Magnetism in condensed matter*. Oxford University Press, 2001.
- [4] G. A. Prinz, “Magnetic metal films on semiconductor substrates,” in *Ultrathin magnetic structures II*, Springer, 1994.
- [5] L. Landau and E. Lifshitz, “On the theory of the dispersion of magnetic permeability in ferromagnetic bodies,” *Phys. Z. Sowjetunion*, vol. 8, p. 153, 1935.
- [6] T. L. Gilbert, “A lagrangian formulation of the gyromagnetic equation of the magnetization field,” *Phys. Rev.*, vol. 8, p. 1243, 1935.
- [7] J. Fassbender, “Magnetization dynamics investigated by time-resolved kerr effect magnetometry,” in *Spin dynamics in confined magnetic structures*, Springer, 2003.
- [8] C. Kittel, “On the theory of ferromagnetic resonance absorption,” *Phys. Rev.*, vol. 73, p. 155, 1948.
- [9] L. Baselgia, M. Warden, F. Waldner, S. L. Hutton, J. E. Drumheller, Y. Q. He, P. E. Wigen, and M. Maryško, “Derivation of the resonance frequency from the free energy of ferromagnets,” *Phys. Rev. B*, vol. 38, p. 2237, 1988.
- [10] M. Buess, T. P. J. Knowles, U. Ramsperger, D. Pescia, and C. H. Back, “Phase-resolved pulsed precessional motion at a schottky barrier,” *Physical Review B*, vol. 69, p. 174422, 2004.
- [11] M. Vomir, L. H. F. Andrade, L. Guidoni, E. Beaupaire, and J.-Y. Bigot, “Real space trajectory of the ultrafast magnetization dynamics in ferromagnetic metals,” *Phys. Rev. Lett.*, vol. 94, p. 237601, 2005.
- [12] H. B. Zhao, D. Talbayev, Q. G. Yang, G. Lupke, A. T. Hanbicki, C. H. Li, O. M. J. van ’t Erve, G. Kioseoglou, and B. T. Jonker, “Ultrafast magnetization dynamics of epitaxial Fe films on AlGaAs (001),” *Appl. Phys. Lett.*, vol. 86, p. 152512, 2005.

Bibliography

- [13] S. D. Bader and J. L. Erskine, “Magneto-optical effects in ultrathin magnetic structures,” in *Ultrathin magnetic structures II*, Springer, 1994.
- [14] G. Woltersdorf, M. Buess, B. Heinrich, and C. H. Back, “Time resolved magnetization dynamics of ultrathin Fe(001) films: Spin-pumping and two-magnon scattering,” *Phys. Rev. Lett.*, vol. 95, p. 037401, 2005.
- [15] E. Beaupre, J.-C. Merle, A. Daunois, and J.-Y. Bigot, “Ultrafast spin dynamics in ferromagnetic nickel,” *Phys. Rev. Lett.*, vol. 76, p. 4250, 1996.
- [16] *See software documentation for MATLAB R2007a.*
- [17] M. Dumm, M. Zölfl, R. Moosbühler, M. Brockmann, T. Schmidt, and G. Bayreuther, “Magnetism of ultrathin FeCo (001) films on GaAs(001),” *J. Appl. Phys.*, vol. 87, p. 5457, 2000.
- [18] M. Brockmann, M. Zölfl, S. Miethaner, and G. Bayreuther, “In-plane volume and interface magnetic anisotropies in epitaxial Fe films on GaAs(001),” *J. Magn. Magn. Mater.*, vol. 199, pp. 384–386, June 1999.
- [19] E. Gu, J. A. C. Bland, C. Daboo, M. Gester, L. M. Brown, R. Ploessl, and J. N. Chapman, “Microscopic magnetization reversal processes and magnetic domain structure in epitaxial Fe/GaAs(001) films,” *Phys. Rev. B*, vol. 51, p. 3596, 1995.
- [20] R. M. Bozorth, “Magnetism,” *Rev. Mod. Phys.*, vol. 19, pp. 29–86, Jan 1947.
- [21] S. Chikazumi, *Physics of Ferromagnetism*. Oxford University Press, 1997.
- [22] P. Bouchon, “Magnetic properties of epitaxial Fe and FeCo films on GaAs (001),” tech. rep., IBM Zurich Research Laboratory, 2007.
- [23] M. Djordjevic, G. Eilers, A. Parge, and M. Münzenberg, “Intrinsic and nonlocal gilbert damping parameter in all optical pump-probe experiments,” *J. Appl. Phys.*, vol. 99, p. 08F308, 2006.
- [24] R. C. O’Handley, *Modern Magnetic Materials: Principles and Applications*. Wiley-Interscience, 2000.